The desmosomal cadherin Desmogon is necessary for the structural integrity of the Medaka notochord

Ali Seleit[1,2, #], Karen Gross[1,2], Michaela Woelk[1,], Camilla Autorino[1], Lazaro Centanin[1,#].

1 Animal Physiology and Development, Centre for Organismal Studies (COS) Heidelberg, Im Neuenheimer Feld 230, Heidelberg 69120, Germany.

2 The Hartmut Hoffmann-Berling International Graduate School of Molecular and Cellular Biology (HBIGS), University of Heidelberg, Heidelberg, Germany.

authors for correspondence: AS, ali.seleit@cos.uni-heidelberg.de and LC, lazaro.centanin@cos.uni-heidelberg.de

Running Title: *desmogon* is necessary for notochord integrity

Abstract

The notochord is an embryonic tissue that acts as a precursor to the spine. It is composed of outer sheath cells and inner vacuolated cells. Together they ensure the ability of the notochord to act as a hydrostatic skeleton until ossification begins. To date, there is still a paucity in our understanding of how the notochord cell types are specified and the molecular players controlling both their formation and maintenance remain poorly understood. Here we report that *desmogon,* a desmosomal cadherin, is essential for proper vacuolated cell shape and therefore correct notochord morphology. We trace *desmogon*+ precursors and uncover an early developmental heterogeneity that dictates the balance of vacuolated and sheath cell formation. We demonstrate that the growth of vacuolated cells occurs cell autonomously and reveal the presence of distinct injury sensing mechanisms in the notochord. Additionally, using a small-scale F0 CRISPR screen we implicate uncharacterized genes in notochordal integrity.

Introduction

The notochord is the defining characteristic that unites all chordates (Lim et al. 2017; Satoh et al. 2012; Stemple 2005; Stemple et al. 1996; Corallo et al. 2018). Developmentally, it derives from the dorsal organizer region in vertebrate embryos (Stemple 2005; Ellis et al. 2013; Corallo et al. 2018). Subsequently, its constituent cells adopt a mesodermal fate and undergo convergent-extension movements (Satoh et al. 2012; Tada & Heisenberg 2012; Corallo et al. 2018; Stemple 2005; Stemple 2004). This results in a tube-like structure that runs along the anterior-posterior axis while simultaneously delimiting the dorso-ventral axis (Stemple 2005). In addition to providing structural support to embryos by acting as the major skeletal element during embryonic development (Stemple et al. 1996; Stemple 2005), it also has important signalling roles (Yamada et al. 1991; Yamada et al. 1993; Pourquie et al. 1993; Hebrok et al. 1998; Fouquet et al. 1997; Corallo et al. 2018; Stemple et al. 1996; Stemple 2005; Satoh et al. 2012). Indeed, patterning of adjacent tissues by the notochord is essential for correct morphogenesis to occur (Yamada et al. 1991; Yamada et al. 1993; Pourquie et al. 1993; Hebrok et al. 1998; Fouquet et al. 1997; Talbot et al. 1995; Stemple et al. 1996; Fleming 2004; Corallo et al. 2018). In vertebrates the notochord is a transient structure and a precursor to spine formation, it is eventually almost entirely replaced by vertebrae (Fleming 2004; Stemple 2005; Corallo et al. 2018; Lopez-Baez et al. 2018; Gray et al. 2014). Recently, it has been shown that correct spine patterning relies on segmentation cues present in the embryonic notochord (Wopat et al. 2018; Lleras Forero et al. 2018). This and other observations has led to the understanding that correct notochord morphogenesis is essential for normal spine formation (Fleming 2004; Lim et al. 2017; Wopat et al. 2018; Lleras Forero et al. 2018; Gray et al. 2014).

The notochord of all vertebrates studied to date (Ellis et al. 2014; Corallo et al. 2018) is formed of two cell-types: an outer sheath epidermal-like cell population and an inner vacuolated cell core (Stemple 2005; Corallo et al. 2018). The outer sheath cells cover the notochord tube and secrete ECM components that help in building and maintaining the peri-notochordal membrane

57 (Ellis et al. 2013; Corallo et al. 2018; Yamamoto et al. 2010; Lim et al. 2017), while the inner-
58 cells have large lysosomally-derived vacuoles that can withstand high hydrostatic pressure
59 (Ellis et al. 2013; Ellis et al. 2014). This ability to act as a hydrostatic skeleton is particularly
60 important in teleost fish as the strength and flexibility of the notochord is essential for proper
61 locomotion – which in turn is necessary for survival – as embryogenesis concludes (Stemple
62 et al. 1996; Ellis et al. 2014; Jiang & Smith 2007). A number of mutants affecting overall
63 notochord formation and differentiation have previously been described in ENU screens
64 (Stemple et al. 1996; Talbot et al. 1995). More recently, new players have been uncovered
65 that are important for vacuolated cell formation and maintenance (Lim et al. 2017; Garcia et
66 al. 2017). However, many decades after the first description of the notochordal cell types, there
67 is still a paucity in our understanding of the molecular players that control the correct formation
68 and maintenance of vacuolated and sheath cells and by extension the structural integrity of
69 the notochord (Ellis et al. 2013).
70
71 Here we uncover new regulators of correct notochord morphogenesis in vertebrates.
72 Desmogleins are a conserved family of calcium-binding cadherin transmembrane proteins.
73 They localize to cellular membranes and are important for establishing strong cell-cell contacts
74 and maintaining tissue integrity (Garrod & Chidgey 2008a). Structurally, they are part of the
75 intercellular desmosome junctions (Garrod & Chidgey 2008a) and are expressed in tissues
76 that undergo significant mechanical strain (Delva et al. 2009). We characterize the role of a
77 fish-specific Desmoglein, hereafter referred to as *desmogon*, that is expressed in the
78 notochord of Medaka and is to our knowledge the first Desmoglein reported to be present in
79 chordate notochords. The loss of *desmogon* causes vacuolated cell defects and leads to
80 structural deformities in the notochord. We generated a Tg(*desmogon*:EGFP) to address the
81 origin and growth dynamics of vacuolated cells by 4D-imaging, a process revealed to be
82 incremental and locally uncoordinated; vacuolated cells behave like autonomous units.
83 Interestingly, *desmogon* also labels early disc-shaped notochord precursors that constitute a
84 bipotent population. When analysed in 4D at the single-cell level, however, we reveal that each

85 progenitor is unipotent and generates either one vacuolated cell or a number of sheath cells.
86 In addition, exploiting the stable labelling of vacuolated cells in our Tg(*desmogon*:EGFP), we
87 uncover two distinct types of regeneration responses in Medaka notochords, one spatially
88 localized and the other global, that depend on the type of injury sustained. Finally, we use
89 Tg(*desmogon*:EGFP) to carry out a small scale reverse-genetics screen on highly conserved
90 and uncharacterized genes enriched in the notochord (Briggs et al. 2018; Farrell et al. 2018).
91 Using this fast and straight-forward methodology we were able to implicate new players in
92 correct notochord morphology in a vertebrate model. This work and approach, we believe,
93 could lead to a deepening of our understanding of the origin of spine and vertebral defects.

Results

***desmogon* is a fish-specific desmosomal cadherin expressed in the notochord**

While searching for a stable marker for neuromast border cells (Seleit et al. 2017) we serendipitously came across a novel uncharacterized *desmog-2-like* gene (ENSORLG00000017110), which we named *desmogon*. The 5.3Kb long transcript of *desmogon* is distributed over 14 exons and encodes a protein with at least 3 desmosomal cadherin domains and one cytoplasmic cadherin domain (Supplementary Figure 1). Based on the amino acid sequence the expected sub-cellular localization is plasma membrane and it is predicted to function as a component of the inter-cellular desmosome junctions. A list of all known orthologues of *desmogon* suggests that this gene is fish-specific, as it is absent in all other sequenced chordates (materials and methods for details) (Supplementary Table 1 and 2). Among fish, the *desmogon* locus is conserved in the vast majority of teleost branches although interestingly, it seems to have been lost in Zebrafish and Tetraodon (as evidenced by the syntenic conservation of the surrounding genomic region) (Supplementary Figure 1). *In situ* hybridization showed *desmogon* to be highly expressed in the developing notochord of Medaka (Figure 1A). To gain a better understanding of the dynamic spatial expression of *desmogon* we generated the Tg(*desmog*:EGFP) (Figure 1B-F) by using a 2.2kb proximal promoter region that contained strong peaks of H3K4 methylation (Supplementary Figure 1). Confocal analysis of mosaic, injected *desmogon*:EGFP and of Tg(*desmogon*:EGFP) medaka embryos revealed EGFP expression in the developing notochord throughout embryogenesis (Figure 1B-F, Supplementary Movies 1 & 2), this expression persists in adult fish in a segmented pattern along the spine (data not shown). Within the notochord, *Desmogon* labels vacuolated cells *(*Figure 1 C, F, arrows in Figure 1E, 1F) and a proportion of covering sheath cells *(*yellow asterisks in Figure 1E, 1F). The expression of a Desmoglein family member in vacuolated and sheath cells suggests the presence of desmosomes in both cell-types, therefore we followed an electron microscopy (EM) approach to characterise the notochord of 10 dpf *wild-type* medaka larvae at the sub-cellular level. Previous studies reported the existence of caveolae in the cellular membrane of vacuolated cells in the zebrafish notochord

123 (Nixon et al., 2007; Lim et. al, 2017), which we confirmed is also present in medaka (Figure
124 1G, G'). Additionally, we observed the occurrence of desmosomes mediating the physical
125 association of neighboring vacuolated cells (Figure 1G, G'), presumably to enhance their inter-
126 cellular adhesion capacities. Desmosomes were also found connecting sheath to vacuolated
127 cells (Figure 1H, I), and sheath to sheath cells (Figure 1I). Altogether, our results reveal the
128 expression of an uncharacterised Desmoglein family member in the two cell types of the
129 notochord that concurrently display desmosomes on their cellular membranes.
130

131 **Vacuolated cells grow as autonomous units**
132
133 The Tg(*desmog*:EGFP) allowed us to follow the axial extension of the notochord as the embryo
134 develops. Notochord expansion was mediated by the growth of vacuolated cells that not only
135 increase in size but also change their circular morphology into a more oblique shape as the
136 notochord matures (Figure 2A, B) (n>10). Using single plane illumination microscopy (SPIM)
137 (Krzic et al., 2012) we observed that vacuolated cells grow anisotropically over time (Figure
138 2C-E, and Supplementary Figure 2) in a process that appears to be irreversible (N>50 cells).
139 Our 4D data also suggests that *desmogon*+ vacuolated cells in medaka are post-mitotic, since
140 we have not detected dividing vacuolated cells in any of our imaging (N=3 embryos at 4 dpf,
141 and N=2 embryos at 3dpf image for 24h, N>50 cells) (Supplementary movie 3). Remarkably,
142 our analysis revealed that vacuolated cells increment their size in a locally uncoordinated
143 manner, where even neighbouring vacuolated cells grow at different rates (Figure 3C-E',
144 Supplementary Movie 4). These results demonstrate that vacuolated cells grow as
145 autonomous units. We next wondered whether the Medaka notochord grows in size just by the
146 increase in volume of vacuolated cells, or if in addition new vacuolated cells are being
147 incorporated. We observed *desmogon*+ precursor cells differentiating into vacuolated cells
148 (Figure 2D-E', Supplementary Movies 5 & 6) in a process that occurred along the notochord.
149 The formation of new vacuolated cells was more frequently observed at the posterior tip of the
150 extending medaka notochord (Figure 2E-E'', Supplementary Movie 6) (Total N=8 cells in 2
151 independent embryos). Our data indicates that during axial extension the number of

152 vacuolated cells increases in the notochord, however, this is not the only cell-type that needs
153 to be amplified during notochord extension. We therefore aimed to better resolve the cellular
154 processes leading to the incorporation of new vacuolated and sheath cells as the notochord
155 grows.
156
157 **Behavioural heterogeneity of notochord precursor cells**
158 In addition to labelling vacuolated and sheath cells in medaka, the (*desmogon*:EGFP) shows
159 expression in early, undifferentiated notochord precursors known as disc-shaped-progenitors
160 (Figure 1B, Figure 3A and Supplementary Movie 7). The population of disc-shaped-progenitors
161 was previously shown to generate both differentiated cell types (Yamamoto et al., 2010), and
162 therefore constitutes a bi-potent population. While analysing sparsely labelled notochords of
163 medaka larvae injected with *desmogon*:EGFP (Figure 3B-C), we noticed that clusters tended
164 to contain either vacuolated or sheath cells (N=41 sheath cells clusters, N=39 vacuolated cell
165 clusters, N=80/93 cell-type specific cluster and N=13/93 clusters containing both cell types,
166 N=93 clusters in 26 mosaic larvae). These results suggest that under physiological conditions
167 disc-shaped progenitors might be bi-potent as a population, but fate-restricted as individual
168 cells. To gain a finer spatial/temporal resolution on the formation of vacuolated and sheath
169 cells in the notochord, we decided to inject the *desmogon*:EGFP construct into zebrafish
170 embryos. Even though a *desmogon* orthologue is not present in this species, we could observe
171 labelled vacuolated and sheath cells in *desmogon*:EGFP zebrafish injected embryos
172 (Supplementary Figure 3, and Supplementary Movie 8), indicating that the transcriptional
173 machinery driving expression of medaka *desmogon* is conserved in distantly related teleosts.
174 Live-imaging on embryos with EGFP+ clones in the notochord revealed that the growth of
175 vacuolated cells is incremental but also locally uncoordinated in Zebrafish (n=6 embryos n>10
176 vacuolated cells) (Supplementary movie 8). Focusing on earlier stages of notochord
177 development, we were able to clearly observe vacuolated and sheath cell formation from
178 undifferentiated *desmogon*+ notochord precursor cells. These disc-shaped precursors were
179 located primarily but not exclusively at the growing posterior tip of the notochord. We observed

180 two distinct, mutually exclusive cellular behaviours in *desmogon*+ precursors. Either they
181 directly generate a single vacuolated cell (Supplementary Movie 9, Supplementary Figure 3,
182 magenta asterisk) (N=9 cells), or they undergo a dorso-ventral symmetric division leading to
183 the formation of sheath cells (Supplementary Movie 9, Supplementary Figure 3, yellow
184 asterisk) (n>10 cells). This behavioural heterogeneity does not seem to be temporally
185 controlled or governed by morphogenetic gradients, since both cellular outcomes can occur
186 simultaneously in neighbouring precursors. Our data shows that disc-shaped *desmogon*+
187 precursors can directly differentiate into vacuolated cells that will not undergo mitosis
188 throughout our imaging (n>10 cells in=6 embryos), while the formation of sheath cells
189 necessitates a symmetric division that could be followed by further amplifying rounds of
190 divisions (n>10 cells in n=6 embryos). Interestingly, we consistently observed that disc-shaped
191 precursors contained a detectable vacuole which was expanded during vacuolated cell
192 differentiation, and lost during the maturation of sheath cells. Indeed, directly after the dorso-
193 ventral symmetric division, a proportion of newly formed sheath cells do contain small vacuoles
194 (n>10 cells in n=6 embryos) (Supplementary Movie 10), suggesting that this feature could
195 reflect an earlier developmental state that must be repressed during the maturation of sheath
196 cells. Although phylogenetically distantly related within the teleost branch, the results from
197 Zebrafish mirrored our findings in Medaka, particularly the non-mitotic nature of desmogon+
198 vacuolated cells. Our results indicate that in both species disc-shaped precursors are
199 exhausted by the end of notochordal development, which raises the question of whether and
200 how vacuolated cells can be replaced after injury of mature Medaka notochords.
201
202 **Vacuolated cell loss triggers a robust and localized regeneration response in medaka**
203
204 Spatially targeted and precise multi-photon laser ablation of 6-10 vacuolated cells of 5-6 dpf
205 Tg*(desmogon:*EGFP*)* embryos resulted in the specific loss of cells in the area of injury (Figure
206 4A, Supplementary movie 11 and 12). Both sheath and vacuolated cells outside the ablated
207 zone retain a normal morphology and the overall integrity of the notochord is unaffected. We
208 next assessed whether a regeneration response can occur in the ablated area. Indeed, 48-
209 hours post injury we observed the appearance of small *desmogon*+ vacuolated cells

210 specifically in the area of injury (Figure 4B, Supplementary movie 13) (n=8 embryos).
211 Interestingly, the overall morphology, presence of a small vacuole, and EGFP+ expression of
212 these cells was highly reminiscent of the earliest vacuolated sheath cells we observed during
213 development in Zebrafish notochords, suggesting that the source of new vacuolated cells is
214 the same in both species (Garcia et al. 2017). The small vacuolated cells grow in size over
215 time as assessed at 5 days post injury (Figure 4C, Supplementary movie 14) (n=8 embryos),
216 this growth followed the same autonomous rationale we observed under physiological
217 conditions in Medaka. Overall, our results indicate that Medaka notochords can mount robust
218 regeneration in response to vacuolated cell loss. This occurs in a highly spatially localized
219 manner that is restricted to the initial injury site.
220
221 **Peri-notochordal membrane injury triggers a global regeneration response**
222
223 The perinotochordal membrane is a thick ECM layer that ensheathes the notochord and helps
224 to maintain its integrity. To test the effect of a sudden loss of hydrostatic pressure within the
225 notochordal tube, we ablated the lower lining of the peri-notochordal membrane (Figure 4D,
226 Supplementary movie 15). Two days post-injury we observed *desmogon*+ cells leaking outside
227 of the notochord tube, indicating that the lower lining of the notochordal membrane failed to be
228 repaired. This in turn led to a loss of notochord morphology and the appearance of small
229 vacuolated cells no longer became restricted to the injury site but were rather spread over the
230 entire tube (Figure 4E). Interestingly, perinotochordal injury and the concomitant lack of repair
231 triggered a global regenerative response even in the absence of vacuolated cell ablation
232 anterior and posterior to the targeted site. Five days post-injury the leakage of notochord
233 vacuolated cells continued and the morphology of the notochord was heavily perturbed. We
234 observed a cluster of *desmogonGFP*+ vacuolated cells ventral to the notochord tube at the
235 site of the original injury, and small vacuolated cells persisted anterior and posterior to the
236 injury site (Figure 4F) (n=3). Overall, we conclude that injury to the peri-notochordal membrane
237 cannot be repaired efficiently in Medaka. This leads to cell leakage and a perturbed notochord
238 morphology, which in turn triggers a global regeneration response that is not spatially restricted
239 to the initial injury site.

240 ***Desmogon* crispants and stable mutants exhibit notochordal lesions of collapsed**
241 **vacuolated cells**
242
243 To test if *desmogon* has any functional role during notochord morphogenesis we designed 3
244 gRNAs targeting different exons along its coding sequence. CRISPR/Cas9 injection into
245 Tg*(desmogon:*EGFP*)* resulted in lesions containing collapsed vacuolated cells along the
246 length notochord, which were absent in embryos injected with control *oca2* gRNAs (Figure 5
247 A-C, Supplementary Movies 16, 17) (Lischik et al. 2018). The vast majority of injected embryos
248 survived until stage 42 and no obvious pleiotropic effects were detected, suggesting the effects
249 observed were notochord specific. Importantly, a proportion of F0 injected embryos that
250 survived to adulthood showed strong signs of bending and defective spine formation (data not
251 shown). The described phenotypes for the F0 injected *desmogon* crispants were consistently
252 recapitulated in *desmogon* mutants (Figure 5D, Supplementary Figure 5, Supplementary
253 Movies 18, 19). To gain a better understanding of the structural phenotypes we decided to
254 perform electron microscopy (EM) on *desmogon* mutants. Longitudinal sections on wild-type
255 notochords were characterised by the typical highly ordered array of vacuolated cells (Figure
256 5E). This contrasts with the structural disorganisation present in lesioned areas of the
257 *desmogon* mutant notochords (Figure 5F-H). EM data also showed the presence of vacuolated
258 cells of appreciably different sizes (Figure 5F, arrows), evidence of vacuolated cell collapse
259 (Figure 5F-G'), and invasion of sheath cells into the central notochord tube that indicates the
260 possible triggering of a regenerative response in the lesioned area (Figure 5F asterisk and
261 Figure 5H, Supplementary Figure 4). Stronger *desmogon* phenotypes included the loss of
262 notochord integrity and shape as revealed by kinking and buckling along the notochord tube
263 (Figure 6A-C). A closer analysis of the phenotypes affecting embryos with collapsed
264 notochords revealed the presence of larger lesions that were consistently filled with
265 *desmogon*+ small vacuolated cells (Supplementary Movie 18 & 19). In addition to being a
266 marker for vacuolated cells, we therefore believe that *desmogon* has a functional role in proper
267 notochord development and shape. Its loss leads to vacuolated cell collapse and the
268 appearance of lesions that contain small vacuolated cells, this can in turn lead to gross
269 morphological defects in the notochord.

270 ***Targeted CRISPR screen uncovers novel regulators of notochord integrity***

271 Realizing the concurrence of F0 CRISPR phenotypes with the ones observed for the stable
272 mutant line, as recently reported for other systems (Wu et al. 2018; Lischik et al. 2018;
273 Trubiroha et al. 2018), we decided to use the Tg*(desmogon:*EGFP*)* as a fast and straight-
274 forward read-out for notochord defects. We searched for putative regulators of notochord
275 integrity by using the recently generated single-cell transcriptome data from Zebrafish (Briggs
276 et al. 2018; Farrell et al. 2018). We selected a number of well annotated and poorly
277 characterized genes that were conserved across vertebrates and highly expressed during
278 Zebrafish notochord morphogenesis (*arrdc3a, kcnk6, pmp22b, si:dkey- 261h17.1 and vgll2b*).
279 We then performed a small-scale F0 CRISPR screen (Wu et al. 2018) in Tg*(desmogon:*EGFP*)*
280 embryos by targeting each selected gene with 2 gRNAs (for details of selection criteria see
281 materials and methods). For *vgll2b* this resulted in 55% of injected embryos showing
282 morphological defects in notochord shape and integrity including twisting and bending of the
283 notochord tube (Figure 6D, F and Table 1). Targeting *arrdc3a* resulted in 30% of injected
284 embryos showing disruption in notochordal integrity, with strong phenotypes including buckling
285 and kinking (Figure 6E, F, and Table 1). Targeting *kcnk6, si:dkey- 261h17.1, pmp22b* with the
286 same approach resulted in strong phenotypes on the notochord but additionally all three
287 showed significant pleiotropic effects (Stemple et al. 1996), including general growth
288 retardation, shorter body axes and gross morphological defects (Table 1). It is therefore more
289 difficult to assign causal phenotypes to these genes. It is clear, however, that they directly or
290 indirectly affect correct notochord morphology. In conclusion, using a straight-forward reverse-
291 genetics approach we have uncovered novel and conserved regulators of notochord
292 morphogenesis and maintenance in vertebrates.

Discussion

Desmogleins are a conserved family of desmosomal cadherins that localize to the plasma membrane of cells (Garrod & Chidgey 2008b; Delva et al. 2009). They are a constituent part of desmosomes and are important mediators of strong inter-cellular adhesion. Indeed, desmosomes have been shown to be expressed in cell types that operate under significant mechanical strain (Garrod & Chidgey 2008b; Delva et al. 2009). Loss of desmosomal function leads to disruption of tissue integrity (Garrod & Chidgey 2008a). The notochord is a tissue that is constantly assailed by strong mechanical stresses (Lim et al. 2017; Garcia et al. 2017; Corallo et al. 2018). It is able to withstand those pressures primarily because of its structural organization: large vacuolated cells on the inside of the tube are surrounded by a strong peri-notochordal membrane formed by sheath cells (Lim et al. 2017; Yamamoto et al. 2010; Koehl et al. 2000; Adams et al. 1990). Our study on *desmogon,* a fish-specific desmosomal cadherin, is the first showing a desmoglein family member expressed and functional in vertebrate notochords.

desmogon **is necessary for correct notochord morphology in Medaka**

The structural demands on teleost notochords are particularly high given that larvae need to swim and feed as soon as embryogenesis concludes (Jiang & Smith 2007; Stemple et al. 1996; Ellis et al. 2014). Significantly, this happens before the ossification and formation of spines (Corallo et al. 2018; Lleras Forero et al. 2018; Wopat et al. 2018; Fleming 2004; Gray et al. 2014). This could explain the specific allocation of this desmoglein family member expression to the notochord. To test whether *desmogon* has a functional role in the Medaka notochord we targeted it by CRISPR/Cas9 and observed flattened vacuolated cells and lesions along the length of the notochord. This could either be a sign of collapsed vacuolated cells (Lim et al., 2017) or a failure of vacuolated cells to properly form. Our EM data on lesioned mutant notochords strongly suggests that the phenotype results from the local collapse of vacuolated cells. Interestingly, in areas that contained larger lesions (both in injected fish and in stable

322 mutants), we consistently observed the appearance of small vacuolated cells. This is highly
323 reminiscent of results we report from the regeneration experiments and suggests that the
324 collapse of *desmogon* mutant vacuolated cells can trigger a regenerative response. Indeed
325 EM results on lesioned notochords shows evidence of invading sheath cells. Our results
326 indicate that *desmogon* is necessary for the maintenance and/or growth, but not the formation,
327 of vacuolated cells. Additionally, we observed a strong correlation between the size of the
328 mutant lesion and the structural integrity of the notochord, bigger lesions invariably led to
329 buckling and kinking of the notochord tube. Our results are in line with previous observations
330 that have shown that correct vacuolated cell morphology is essential for the notochord to
331 withstand the high mechanical stresses it faces (Lim et al. 2017; Ellis et al. 2013; Garcia et al.
332 2017; Fleming 2004; Adams et al. 1990). Failure of properly building up and maintaining the
333 high hydrostatic pressure inside the notochord tube leads to bending and buckling along the
334 length of the notochord (Ellis et al. 2013; Corallo et al. 2018). Our results demonstrate that the
335 presence of *desmogon* in the Medaka notochord is necessary for correct vacuolated cell shape
336 and by extension proper notochord morphology and integrity.
337
338 The fact that *desmogon* is present in the vast majority of teleost branches argues that it has a
339 conserved role in notochord maintenance in fish. However, there are two intriguing exceptions,
340 *desmogon* has no detectable orthologues in Tetraodon or in Zebrafish. It seems likely that both
341 fish have lost *desmogon* through the course of their evolution, this interpretation is supported
342 by the fact that we can identify syntenic genomic regions that do not contain *desmogon.* It
343 remains a formal possibility, however, that an orthologue with a highly divergent nucleotide
344 sequence exists in Zebrafish and Tetraodon. It would be interesting to see whether other
345 desmosomal cadherins have taken over the notochordal role of *desmogon* in those species.
346 Indeed, other desmosomal cadherin family members have been implicated in notochord
347 integrity in Zebrafish (Goonesinghe et al. 2012), although mutants display earlier gastrulation
348 defects that complicate the proper characterisation of notochordal phenotypes. Interestingly,
349 injecting our medaka *desmogon* partial promoter driving GFP in Zebrafish results in vacuolated

350 and sheath cell labelled clones. This suggests that the core transcriptional machinery driving
351 tissue-specific expression of *desmogon* remains in place and active in Zebrafish. It would be
352 of interest to investigate when the deployment of desmosomal cadherins in notochords arose
353 during evolution and how wide-spread its usage is among the different chordate clades.
354
355 ***Tg(desmogon:EGFP)*as a screening tool for genes involved in proper notochord**
356 **morphology**
357
358 It has been reported that most biomedical research today focuses heavily on a limited number
359 of genes, leaving behind potentially important genes understudied (Stoeger et al. 2018).
360 Making use of our newly generated transgenic line in combination with the recently published
361 and publicly available single cell transcriptomics data from vertebrate embryos (Briggs et al.
362 2018; Farrell et al. 2018), we attempted to address this imbalance. To do so we performed a
363 small scale F0 CRISPR screen, the efficacy of which has been recently demonstrated in
364 Zebrafish (Wu et al. 2018) and confirmed in other fish species (own observations and personal
365 communications). Indeed, recent work in Medaka (Lischik et al. 2018), in addition to our results
366 from *desmogon* mutants, argues for the use of F0 injected embryos as a method to analyse
367 tissue-specific phenotypes. Briefly, we focused on conserved well-annotated genes that were
368 highly and differentially expressed in developing notochords. We addressed whether they
369 might be involved in proper notochord morphology by using the *desmogon:GFP* line as a fast
370 and straight-forward read-out for notochord shape and integrity. Broadly, the targeted genes
371 fell into two categories. *kcnk6, si:dkey- 261h17.1, pmp22b* constituted the first category and
372 showed strong pleiotropic effects in addition to notochordal defects. Delineating the cause of
373 the pleiotropy is difficult given the essential signalling role of the notochord. (Yamada et al.
374 1991; Yamada et al. 1993; Pourquie et al. 1993; Hebrok et al. 1998; Fouquet et al. 1997;
375 Corallo et al. 2018; Stemple et al. 1996). The observed defects could either arise from the
376 inability of the notochord to correctly pattern adjacent tissue or from notochord independent
377 roles for these genes during embryogenesis. This makes assigning causal phenotypes more
378 difficult. The second group of targeted genes contained the conserved putative co-
379 transcriptional factor *vgll2b* and the highly conserved membrane bound arrestin *arrdc3a.* Both

genes showed specific defects in notochord morphology and structure when targeted and no overt pleiotropic phenotypes. This argues for functional roles for these genes that are likely to be notochord specific. The precise cellular defects caused by these two genes remain unclear although in both cases vacuolated cells appeared morphologically normal. It is clear, though, that targeted notochords appear unable to withstand the high mechanical strain and buckle under pressure. It remains a challenge for the future to decipher the genetic networks of these genes and to assess whether their roles are functionally conserved in higher vertebrates. All in all, using a simple, targeted, reverse-genetics approach, in combination with publicly available data from single cell transcriptomics (Briggs et al. 2018; Farrell et al. 2018), we believe we have implicated new players in correct vertebrate notochord integrity. This methodology can be easily adapted to other contexts and promises to aid in the study of neglected genes with potentially important functions.

Notochord vacuolated cells during development

We made use of the newly generated *Tg(desmogon:EGFP)* line to address the formation and growth dynamics of notochord vacuolated cells during development. It has previously been reported that one vacuole exists per vacuolated cell under homeostatic conditions (Ellis et al. 2014) and therefore vacuole growth can be used as a proxy for cellular volume growth. Our results confirm that vacuolated cells grow in volume over time as has been reported before (Ellis et al. 2013; Ellis et al. 2014) and reveal that they do so anisotropically, changing their morphology in the process from more roundish to more oblique shapes. This might be due to the increased cellular packing as the notochord expands. While it has been previously shown that notochords extend over time and that this supports axis elongation in vertebrate embryos (Ellis et al. 2014; Garcia et al. 2017; Ellis et al. 2013), it is still unclear exactly how this growth and expansion is coordinated. A possible mechanism could be that a morphogen gradient synchronizes the growth of neighbouring cells in an orderly fashion. Our dynamic data, in both medaka and zebrafish embryos, argues against the presence of such a signal. We reveal that the growth of vacuolated cells in Medaka and Zebrafish is an incremental one-way process

410 that is locally uncoordinated; neighbouring vacuolated cells grow at different rates. This
411 strongly suggests cell-autonomous mechanisms of vacuolated cell growth, how this is
412 coordinated globally to eventually reach an equivalent size remains unclear and constitutes an
413 interesting avenue for future research. It could be that the final size reached is close to the
414 physiological limit as has been previously suggested (Ellis et al. 2014).
415
416 In addition to incrementing their size cell-autonomously we report that the number of
417 vacuolated cells increases as the notochord grows. However, in line with previous
418 observations from Zebrafish (Garcia et al. 2017), we have observed no cell division of
419 vacuolated cells. To characterize the initial steps of vacuolated cell formation during notochord
420 development we employed a highly temporally resolved 4-D approach. We observed that
421 vacuolated cells arise from disc-shaped precursors as previously reported (Melby et al. 1996;
422 Dale & Topczewski 2011). Sparse labelling of these *desmogon*+ precursors in developing
423 Zebrafish notochords combined with long-term live-imaging revealed a hitherto unrecognized
424 *in vivo* behavioural heterogeneity of the disc-shaped precursors. Either they directly
425 differentiate into vacuolated cells (forgoing any division), or they generate sheath cells by
426 undergoing a dorso-ventral symmetric division, that could be followed by further amplifying
427 rounds of mitosis. When considering the position along the AP axis, the developmental time
428 and the levels of EGFP+ expression, we were unable to reliably predict the output of a
429 precursor cell. It seems plausible therefore that the decision to form a vacuolated or sheath
430 cell is not predetermined nor controlled by tissue-level morphogens, but rather depends on
431 sensing the needs of the growing notochord tube in a local manner. Indeed, it has been
432 previously reported that Notch-Jag1 signalling is important in the balance between vacuolated
433 and sheath cell formation (Yamamoto et al. 2010), suggesting that fate acquisition could be
434 resolved locally among neighbouring cells. Complementarily, it is possible that local
435 mechanical forces that arise during the expansion of the tube could operate on inherently
436 plastic disc-shaped precursors and contribute to adopting vacuolated or sheath cell identity.
437
438

439
440
441 **Notochord vacuolated cells in regeneration**
442
443 It has been recently shown that Medaka hearts and retinas have a vastly reduced regenerative
444 potential as compared to Zebrafish (Lust & Wittbrodt 2018; Ito et al. 2014; Lai et al. 2017).
445 However, we have previously reported that Medaka neuromasts are able to regenerate
446 efficiently (Seleit, et al. 2017), and the same happens after mechanical amputations on the
447 caudal fin (Katogi et al. 2004) and injuries to the liver (Van Wettere et al. 2013). It therefore
448 seems that Medaka has a highly variable tissue-specific regenerative capacity (Kang et al.
449 2016). We wondered whether Medaka can regenerate lost notochord vacuolated cells. It has
450 been shown in Zebrafish that loss of *caveolae* mutant vacuolated cells in response to
451 mechanical strain triggers an efficient regeneration response (Garcia et al. 2017). This is
452 mediated by sheath cells that invade the inside of the notochord tube and trans-differentiate
453 into vacuolated cells (Garcia et al. 2017). Localized laser-ablation of vacuolated cells in
454 Medaka leads to a very similar process as in Zebrafish where small vacuolated cells
455 specifically invade the injury site. Interestingly, these invading cells start growing in size cell-
456 autonomously mirroring the un-coordinated nature of growth that we observe for vacuolated
457 cells during development. The appearance of small vacuolated cells during regeneration is
458 another reminiscent feature of what we report during notochord development. Indeed, a
459 proportion of sheath cells formed from dividing precursors do initially contain small vacuoles
460 that highly resemble the cells participating in the regenerative response. This suggests two
461 things; a) the presence of sub-populations of sheath cells that display distinct behaviours both
462 during development and regeneration (Lopez-Baez et al. 2018), b) sheath cells participating in
463 the regenerative response most likely re-acquire a small vacuole and could thus be reverting
464 to an earlier state in their developmental history. Reactivation of developmental programs has
465 been a hallmark of efficient regeneration in a variety of models (Tanaka & Galliot 2009; Rodrigo
466 Albors et al. 2015; Kaloulis et al. 2004) and it seems likely that this takes place in the notochord
467 of Medaka after vacuolated cell loss.
468

469 The highly specific spatially localized response to vacuolated cell injury we observe in Medaka
470 indicates that there are mechanisms in place that can sense injured tissue without the need to
471 activate a global regeneration program (LoCascio et al. 2017). Indeed, it has been shown that
472 the release of vacuolated cell contents upon apoptosis can trigger a local regenerative reaction
473 from neighbouring sheath cells (Garcia et al. 2017). A similar process can therefore be
474 occurring in Medaka. Interestingly, when we ablated a small part of the peri-notochordal
475 membrane this led to vacuolated cell leakage at the injury site. As the vacuolated cell leakage
476 continued we witnessed the activation of a global regenerative response anterior and posterior
477 to the original injury site. This could be observed by the presence of small vacuolated cells
478 along the entire length of the notochord. It therefore seems likely that sheath cells can also
479 respond to injury without specific vacuolated cell death, suggesting that sheath cells might be
480 able to sense other stresses like tissue tension. It has recently been reported in Zebrafish that
481 a *wilms*+ subpopulation of sheath cells gets activated in response to a coarse needle injury to
482 the notochord (Lopez-Baez et al. 2018). This sub-population mainly forms scar-tissue that acts
483 as a stopper to maintain notochordal integrity (Lopez-Baez et al. 2018). In Medaka, leakage
484 of vacuolated cells at the site of injury indicates that the peri-notochordal membrane was not
485 efficiently repaired. It is tempting to speculate that this is due to the absence or delayed
486 activation of the wilms+ subpopulation of sheath cells. Overall, our results strongly argue for
487 the presence of distinct injury-sensing mechanisms in sheath cells (dependent and
488 independent of vacuolated cell death). We also report the existence of two regenerative
489 responses in Medaka notochords, one spatially localized and the other global, that depend on
490 the type of injury sustained. Our data positions vacuole re-acquisition by sheath cells as the
491 key step for replenishing vacuolated cells regardless of the type of injury sustained. Identifying
492 the molecular trajectories sheath cells traverse will allow a better understanding of the existing
493 heterogeneities among and plasticity of sheath cells both during development and
494 regeneration. This will in turn allow a more targeted exploitation of the potential of sheath cells
495 in treating notochordal and by extension spinal cord defects in vertebrates.

Figure Legends

Figure 1 d*esmogon* is a desmosomal cadherin that labels the notochord throughout embryogenesis in Medaka.

(A) *in-situ* hybridization on *desmogon* in stage 33 medaka embryos reveals strong enrichment in the notochord. Scalebar=20 microns (B) mosaic injection of desmogon:EGFP in medaka embryos stage 30, labels the notochord . Scale bar=100um (C-D) Transgenic line *Tg(desmog:EGFP)* labels the notochord in Medaka at stage 42 embryos. Scalebar=100 microns (E-F) Maximum projection of mosaic injected (E) and *Tg(desmog:EGFP)* (F) labelling notochord vacuolated cells and a proportion of covering sheath cells. Magenta arrows indicate vacuolated cells and yellow asterisks sheath cells. Scalebar= 50 microns (G) Longitudinal EM section in between vacuolated cells connected by desmosomes (black asterisk) Scale bar= 1 micron (G') Desmosomal structure and caveolae present between vacuolated cells Scale bar = 0.2 micron. (H) Longitudinal EM section showing desmosomal connections between sheath cells and vacuolated cells scale bar= 1 micron. (I) Cross-section EM showing desmosomal connections between two sheath cells in addition to desmosomes between sheath cells and vacuolated cells scale bar= 1 micron.

Supplementary movie1 *Tg(desmog:EGFP)* stage 42 Medaka embryo. Z-stack shows labelled vacuolated cells throughout the notochord and a proportion of sheath cells labelled. Scalebar=100 microns.

Supplementary movie2 *Tg(desmog:EGFP)* stage 42 Medaka embryo. 3D projection shows the specific labelling of the notochord tube by 2.2kb *desmogon* promoter region. Scalebar=100 microns.

525 **Figure 2** Live-imaging of *Tg(desmog:EGFP)* reveals Medaka notochord growth dynamics.
526 (A) Single plane of 3-4dpf *Tg(desmog:EGFP)* embryo showing vacuolated cells, notice more
527 circular shape and small size compared to (B) 5-6dpf *Tg*Desmogon::EGFP, bigger and oblique
528 vacuolated cells. n>10. Scalebar=50 microns. (C-C'''') SPIM time-lapse imaging *of desmogon+*
529 vacuolated cell growth over time highlighted with yellow and magenta asterisks (n>10
530 vacuolated cells in 3 embryos at 4-5dpf and n>10 vacuolated cells in 2 embryos at 3-4dpf).
531 Scalebar=20microns. (D-D'''') Differentiation of desmogon+ precursors into vacuolated cells
532 near mid-point of notochord. Arrow labels cell of interest. (E-E') Differentiation of a number of
533 desmogon+ precursors into vacuolated cells near tip of the tail and growing notochord
534 (magenta asterisks). Scalebar=20 microns. Time in hours. Total n=8 sheath cells in 2
535 independent embryos.
536
537 **Supplementary movie3** *Tg(desmog:EGFP)* 4-5dpf embryo.Time-lapse imaging of developing
538 notochord. No observable divisions of *desmogon+* vacuolated cells. n=3 embryos at 4-5dpf
539 and n=2 embryos at 3-4dpf. Scalebar=20 microns. Time in hours.
540
541 **Supplementary movie4** *Tg(desmog:EGFP)* 4-5dpf embryo. Time-lapse imaging of growing
542 *desmogon+* vacuolated cells. Notice the anisotropic and autonomous nature of vacuolated cell
543 growth, n>10 vacuolated cells in 3 embryos at 4-5dpf and n>10 vacuolated cells in 2 embryos
544 at 3-4dpf. Scalebar= 20microns. Time in hours.
545
546 **Supplementary movie5** *Tg(desmog:EGFP)* 4-5dpf embryo. *desmogon+* precursor
547 differentiates into vacuolated cells that grow in size over time near notochord mid-point.Time
548 in hours. SPIM-imaging. Scalebar=20 microns.
549
550 **Supplementary movie6** *Tg(desmog:EGFP)* 4-5dpf embryo near extending posterior end of
551 the tail. *desmogon+* precursors differentiate into vacuolated cells that grow in size over
552 time.Time in hours. SPIM-imaging. Scalebar=20 microns.

553

554 **Supplementary movie7** 3-D reconstruction of *desmog:EGFP injected 3*dpf embryo near
555 extending posterior end of the tail. Notice the labelling of undifferentiated disc-shaped
556 progenitors.

557

558 **Supplementary movie8** Clones of *desmogon*+ cells in 24hpf Zebrafish embryo developing
559 notochord. Both sheath cell clones and vacuolated cell clones are present. Notice the growth
560 of vacuolated cells is locally uncoordinated in Zebrafish as is the case in Medaka. Scalebar=30
561 microns. Time in hours.

562

563 **Supplementary movie9** Clones of *desmogon*+ disc shaped precursors in 24hpf Zebrafish
564 embryo developing notochord. Direct differentiation of the anterior disc-shaped precursor into
565 a vacuolated cell. Posterior disc shaped precursor produces two sheath cells after a dorso-
566 ventral division Scalebar=30 microns. Time in hours.

567

568 **Supplementary movie10** Clones of *desmogon*+ disc shaped precursors in 24hpf Zebrafish
569 embryo. Notice the presence of small vacuoles in newly formed sheath cells, that disappear
570 over time. Scalebar=30 microns. Time in hours.

571

572 **Figure 3 Bi-potent disc-shaped precursor population is fate-restricted at single cell level**
573 (A) Mosaic injected medaka embryo *desmog:EGFP* showing the presence of disc-shaped
574 precursors at the posterior tip of the growing notochord tube. (B-C) independent clones of
575 sheath cells and vacuolated cells occur in mosaic injected fish. (D) Disc-shaped precursors at
576 the growing tip of the medaka notochord are fate-restricted and either generate vacuolated
577 cells or sheath cells. Scale bars are 20um in A, 1mm in B, and 100um in C.

578

579 **Figure 4 Local and global regeneration dynamics after notochord injury**
580 (A)*Tg(desmog:EGFP)* 6dpf embryo post ablation. Ablation area indicated by magenta lines.

581 Vacuolated cells in the ablated zone are missing. Vacuolated cells outside ablation zone are
582 intact and morphologically normal. Scalebar= 100 microns. (B) Same embryo 48 hours post
583 injury. Notice the appearance of small vacuolated cells specifically in the ablated zone.
584 Regeneration of injured area is initiated. Vacuolated cells in uninjured area appear normal.
585 Scalebar= 100 microns. (C) Same embryo 5 days post injury vacuolated cells grow in size,
586 notochord is intact. Scalebar= 100 microns. n=8 embryos. (D) Ablation of vacuolated cells and
587 lower lining of notochord tube. (E) 48 hours post injury, magenta arrow highlights position of
588 injury, notice failure to regenerate and leakage of *desmogon*+ cells outside of notochord.
589 Overall notochord morphology grossly altered both anterior and posterior to injury site. Notice
590 appearance of small vacuolated cells outside original injury site. Scalebar= 100 microns. (F) 5
591 days post injury magenta arrow highlights growing leakage of *desmogon*+ vacuolated cells
592 outside of the notochord. Failure to repair and correctly regenerate lower tube lining is evident.
593 Gross morphological defects apparent over entire length of notochord. Notice the appearance
594 of small vacuolated cells throughout the notochord. Scalebar= 100 microns. n=3 embryos.
595
596 **Supplementary movie11** *Tg(desmog:EGFP)* 6dpf embryo. Pre-Ablation stack through
597 notochord. Scalebar= 100 microns.
598
599 **Supplementary movie12** *Tg(desmog:EGFP)* 6dpf embryo. Post-ablation stack through
600 notochord. Notice the loss of vacuolated cells anteriorly at the site of injury. Scalebar= 100
601 microns.
602
603 **Supplementary movie13** *Tg(desmog:EGFP)* embryo. 48hours post-injury stack through
604 notochord. Small vacuolated cells appear specifically in the site of injury. Scalebar= 100
605 microns.
606
607 **Supplementary movie14** *Tg(desmog:EGFP)* embryo. 5 days post-injury stack through
608 notochord. Vacuolated cells grow in size specifically in the site of injury. Scalebar= 100

609 microns.

610

611 **Supplementary movie15** *Tg(desmog:EGFP)* embryo. Post-ablation stack through notochord.
612 Vacuolated cells and lower lining of notochord ablated. Scalebar= 100 microns.

613

614 **Figure 5 *desmogon* mutants exhibit notochordal lesions and vacuolated cell collapse.**
615 (A)Control CRISPR injected *Tg(desmog:EGFP)* with o*ca2* gRNA1,2 & Cas9. Single plane.
616 Scalebar=100 microns. (B, C) *desmogon* gRNA1, 2, 3 & Cas9 injected into
617 *Tg*Desmogon:E:GFP results in local collapse of vacuolated cells and lesions in the notochord.
618 Single plane. Scalebar=100 microns. (D) Stable desmogon CRISPR mutant line recapitulates
619 phenotypes observed in the injected generation Scalebar=100microns. (E) Longitudinal EM
620 section through wild-type stage 42 medaka notochords with highly ordered vacuolated cell
621 arrangement (F) Longitudinal EM section through lesioned *desmogon* mutant stage 42
622 notochords, notice the structural disorganization, vacuolated cells with varying sizes (yellow
623 arrows), invading sheath cells (black asterisk) and evidence of collapsed vacuolated cells. (G-
624 G') Longitudinal EM section on *desmogon* mutant notochords reveals the presence of
625 collapsed vacuolated cells. (H) Small vacuolated cells are present in Longitudinal sections of
626 EM in *desmogon* mutants and can be clearly distinguished from the neighboring vacuolated
627 cells and sheath cell.

628

629 **Supplementary movie16** *Tg(desmog:EGFP)* 6-7dpf *oca2* gRNA1,2+ Cas9 injection. Z-stack
630 through notochord. Notice normal notochord and vacuolated cell morphology. Scalebar= 100
631 microns.

632

633 **Supplementary movie17** *Tg(desmog:EGFP)* 6-7dpf Desmogon gRNA1,2,3 & Cas9 injection.
634 Z-stack through notochord. Local collapses of vacuolated cells are evident and vacuolated cell
635 morphology is highly perturbed. Scalebar= 100 microns.

636

637 **Supplementary movie18** *Tg(desmog:EGFP)* 6-7dpf desmogon gRNA1,2,3 & Cas9 injection.
638 Z-stack through notochord. Strong phenotypes show abnormal notochord lesions. Notice the
639 presence of small vacuolated cells and cellular debris. Overall a disorganized notochord
640 structure is evident. Scalebar= 50 microns.
641
642 **Supplementary movie19** *Tg(desmog:EGFP)* 6-7dpf desmogon F1 mutant. Z-stack through
643 notochord. Strong phenotypes show abnormal notochord lesions. Phenotype resembles what
644 is observed in the injected generation. Scalebar= 30 microns.
645
646 **Figure 6 Gross morphological defects in the notochord of *desmogon, vgll2b and***
647 ***arrdc3a* CRISPR injected embryos**
648 (A) Overall morphology of control *oca2* gRNA & Cas9 injected notochord in
649 *Tg(desmogon:EGFP)*(B, C) Strong phenotypes in *desmogon* CRISPR injections results in
650 gross morphological defects in notochord integrity and notochord buckling and bending.
651 maximum projections. Scalebar=100 microns. Embryos with notochord phenotypes 65/160.
652 Over 90% of embryos survive to stage 42. (D, F) *vgll12b* gRNA1,2 & Cas9 injected into
653 *Tg(desmog:EGFP)* results in morphological defects in the notochord. Notice magenta arrow
654 where notochord is twisted, overall notochord bending observed. Scale bar=100microns.
655 Embryos with phenotypes in notochord 66/120. 79% of embryos survive to stage 42. (E, F)
656 *arrdc3a* gRNA1,2 & Cas9 injected into *Tg(desmog:EGFP)* results in notochord bending.
657 Scalebar=100microns. Embryos with phenotypes 29/97. 77% of embryos survive to stage
658 42.
659
660 **Table 1** List of genes targeted by CRISPR and quantification of phenotypes in F0 injections.
661
662 **Supplementary Table 1** List of all available species with known orthologues to Medaka
663 d*esmogon* ranked from the highest identity score to the lowest using the 1-1 and 1-many
664 ortholouges comparison. The gene seems to be fish-specific. (ENSEMBLE).

665 **Supplementary Table 2** List of all available species without any othrologues to Medaka
666 *desmogon.* Notice the absence of an orthologous gene in Zebrafish and the Tetraodon
667 (highlighted in magenta). (ENSEMBLE).
668
669 **Supplementary Table 3** List of all available species with known orthologues to Medaka vgl12b
670 ranked from the highest identity score to the lowest. The gene is highly conserved in
671 vertebrates (ENSEMBLE).
672
673 **Supplementary Table 4** List of all available species with known orthologues to Medaka
674 arddc3a ranked from the highest identity score to the lowest. The gene is highly conserved in
675 vertebrates(ENSEMBLE).
676
677 **Supplementary Figure 1** (A) Pfam predicted *desmogon* protein domains. In green, 3 cadherin
678 domains and in red, a cytoplasmic cadherin domain. Multiple sequence alignment of 12
679 selected species to uncharacterized Medaka protein(H2MRM9). Identity score reveals weak
680 amino acid sequence conservation with closest hits (B) Comparative genomic alignment of
681 uncharacterized medaka transcript(ENSORLG00000017110) using GENOMICUS shows
682 conservation of locus in the vast majority of teleost branches, notice the loss of locus in
683 Zebrafish and the Tetraodon. Locus of interest is highlighted by black desmogon label.
684 Scheme modified from Genomicus to highlight syntenic geneomic region (C) Choosing of
685 *desmogon* partial promoter. 2.2kb promoter region (highlighted in blue). H3K27ac, H3K4me1
686 and H3K4me2 peaks from UCSC genome browser Medaka blastula stage data at 2.2kb
687 upstream of predicted *desmogon* TSS.
688
689 **Supplementary Figure 2**
690 (A)Area measurement on 12 paired vacuolated cells at 4 different time-point over a 20-hour
691 period reveals the autonomous nature of vacuolated cell growth. Neighbouring vacuolated
692 cells share the same colour code and grow at different rates. Area was calculated on maximum

693 projections using standard Fiji software.

694

695 **Supplementary Figure 3**

696 (A, A') Time-lapse recording of clones of vacuolated cells (purple asterisks) and sheath cells
697 (yellow asterisks) labelled after injection of desmogonGFP plasmid into Zebrafish embryos.
698 Notice the growth of vacuolated cells over time is asynchronous. (B,B') Time-lapse recording
699 of notochord disc-shaped precursor cells labelled in injected zebrafish embryos. One labelled
700 precursor directly trans-differentiates into vacuolated cell (purple asterisks) while the other
701 undergoes a dorso-ventral division giving rise to two sheath cells (yellow asterisks). Scale
702 bar= 30 microns. Time in hours.

703

704 **Supplementary Figure 4** (A) Longitudinal EM section in *desmogon* mutant notochord.
705 Notice the sheath cell invasion to the center of the lesioned tube Scale bar= 5 microns. (B)
706 High magnification on sheath cell nucleus from (A). Scale bar= 1 micron.

707

708 **Supplementary Figure 5** (A) Single Z plane projection in a Tg(desmogon:EGFP) stage 42
709 embryo, notice the organization and size of vacuolated cells. (B) 3 consecutive Z plane
710 projections in an F1 CRISPR *desmogon* mutant stage 42 embryo, notice the appearance of
711 lesions full of small vacuolated cells (C) Multiple sequence alignment of 9 selected species to
712 uncharacterized Medaka protein *vgll2b*. Identity score reveals very strong amino acid
713 sequence conservation in vertebrates. (D) Multiple sequence alignment of 10 selected
714 species to uncharacterized Medaka protein *arrdc3a*. Identity score reveals very strong amino
715 acid sequence conservation across vertebrates.

716

717

718

719

720

721

Materials and Methods

Fish stocks and generation of transgenic lines

Medaka (*Oryzias latipes*) and Zebrafish (*Danio rerio*) stocks were kept in a fish facility built according to the local animal welfare standards (Tierschutzgesetz §11, Abs. 1, Nr. 1) as described before (Seleit et. al, 2017). Animal experiments were performed in accordance with European Union animal welfare guidelines.(Tierschutzgesetz 111, Abs. 1, Nr. 1, Haltungserlaubnis AZ35–9185.64 and AZ35–9185.64/BH KIT).

The strain used in this study is: Cab (medaka Southern wild type population). Tg(*desmogon*:EGFP) transgenic line was generated for this study by I-SceI mediated insertion, as previously described(Rembold et al. 2006). Briefly, a 2.2kb promoter region upstream of the desmogon CDS (but including the ATG of the first exon) was amplified from Medaka genomic DNA using forward primer (TCGCTGCTTGTTGTGTAGGT) and reverse primer (CATTGGCGCAGTGATTTGAA). The amplified fragment was subsequently cloned by A-tailing into a PGEMTeasy vector (Promega). From there it was sub-cloned into a vector with I-SceI sites and eGFP. This was then injected into Medaka embryos to obtain the transgenic line Tg(*desmogon*:eGFP).

Imaging and Image analysis

Embryos were prepared for live-imaging as previously described (Seleit, et al. 2017a; Seleit, et al. 2017b) 20 mg/ml as a 20x stock solution of tricaine (Sigma-Aldrich, A5040-25G) was utilized to anaesthetise embryos. Glass-bottomed dishes (MatTek Corporation, Ashland, MA 01721, USA) contained the embryos that were in turn covered with low melting agarose (0,6% in ERM). Embryos were screened using an Olympus MVX10 binocular coupled to a Leica DFC500 camera. For image acquisition we used confocal microscopes Leica TCS SPE and Leica TCS SP5 II. Developing notochords were imaged for approximately 1 day using EMBL MuVi-SPIM (Krzic, Gunther, Saunders, Streichan & Hufnagel 2012b) with two illumination

751 objectives (10x Nikon Plan Fluorite Objective, 0.30 NA) and two detection objectives (16X
752 Nikon CFI LWD Plan Fluorite Objective, 0.80 NA). Embryos were placed in glass capillaries
753 using 0,6% low melting agarose at room temperature. Standard Fiji software was used for all
754 image analysis. Stitching was performed using 2D and 3D plugins on Fiji. For mosaic analysis,
755 a *desmogon*:EGFP plasmid was injected embryos into 2 to 4 cell-stage embryos, which were
756 grown until day 9 pf. For the quantification, we selected embryos bearing 1 and up to 4 clusters
757 in the notochord, where clusters were defined as single cells or groups of cell that were at least
758 one somite away from each other.
759

760 **Multi-photon Laser Ablations**

761 A multi-photon laser was used in combination with a Leica TCS SP5 II microscope to perform
762 ablations on vacuolated cells of the notochord and the peri-notochordal membrane in
763 Tg(desmogon:eGFP). 'Point ablations' were chosen along the perimeter of each vacuolated
764 cell. Laser of 880 nm wavelength was used and the power used ranged from 30-35% for 500ms
765 (the time parameter was adjusted in the biological replicates when necessary). The targeted
766 area was immediately imaged post-ablation to checked for signs of cellular bursting, debris
767 and the release of GFP signal.

768 **CRISPR gRNAs and Cas9**

769 Lab-made Cas9 mRNA was transcribed by mMachine Sp6 Transcription Kit (Thermo Fisher).
770 The gRNAs for all targeted genes were designed in-silico using CCtop (Stemmer, Thumberger,
771 et al. 2015). gRNA synthesis was done as previously reported (Stemmer, Thumberger, et al.
772 2015). All genes were targeted with 2 gRNAs against the CDS except *desmogon* where 3
773 gRNAs were designed and injected. The following is a list of gRNA sequences used in this
774 study for each gene.

775 *desmogon gRNA1 (CCCAUAUGGUGUGUUCAGCGUGG) gRNA2*
776 *(UUGGUGCCAGCUCUUCAGCGGGG) gRNA3 (AUCUAUGACUAUGAAGGUCGAGG)*

777 *vgll2b gRNA 1 (UGGGCCCCCAGACAUUCCUUCGG)*

778 *gRNA2(GGGUGCGCCCGUUUCACAGUGGG)*

779 *arrdc3a gRNA1(AAGUUCGUUGGACGGAAUCGAGG)*

780 *gRNA2(AUCCCGCAUGGUGGUCCCAAAGG)*

781 *kcnk6 gRNA1 (GUUCUCCAGCAUCGAGCGGCCGG) gRNA2*

782 *(UGUAUUGUAGUCGCCGGGCGAGG)*

783 *si:dkey- 261h17.1 gRNA1 (GAGCUUGCUGUCACAAGCCUUGG)*

784 *gRNA2(CUGAGUCACUUCAAUCUGCCUGG)*

785 *pmp22b gRNA1(CCUGCUGCACAUUGCUGCACUGG) gRNA2*

786 (CAGCUCUUCACCUUGCAGAAGGG)

787

788 Tg(*desmogon*:eGFP) were injected at the 1 cell stage with a solution containing 15 ng/µl of

789 each gRNA for each gene individually and 150 ng/µl of CAS9 mRNA. The embryos were

790 screened iteratively over the course of development for gross morphological phenotypes and

791 for phenotypes in the notochord. For control injections two gRNAs targeting the *Oca2* locus

792 and Cas9 (Lischik et al. 2018) were injected into Tg(*desmogon*:eGFP) embryos. The stable

793 *desmogon* F2 mutants exhibited a small deletion in the region of guide RNA2.

794

795 **Whole-mount *in-situ* hybridization**

796 A 604bp *in situ* probe for *desmogon* was generated from total cDNA of stage 33 medaka

797 embryos by PCR using the following primers fwd: TTCTGCGAGATCAGGCTCAC rev:

798 AAGGCCCCTCCTCTGTAACT and subsequently A-tailed and cloned into a PGEMTeasy

799 vector (Promega). Sense and anti-sense probes were generated using Sp6 and T7

800 polymerases (Invitrogen) and the In situ hybridization protocol was followed as previously
801 reported in (Stemmer, Schuhmacher, et al. 2015). Hybridisations were performed overnight at
802 65°C then samples were incubated with an antibody against anti-digoxigenin conjugated with
803 AP Fab fragments (1:2000; Roche, 11093274910). Staining was done using NBT/BCIP
804 (Roche).

805 **Electron Microscopy sample preparation and imaging**

806 10 dpf fish from Medaka wt Cab strain and stable Desmogon mutants were placed in a fixative
807 consisting of 2.5% glutaraldehyde and 4% paraformaldehyde in 0.1M PHEM buffer. The
808 fluorescing part of the notochord in mutant fish and equally small pieces of the wt fish was cut
809 out in the fixative and fixation was continued for 30 min at room temperature and at 4˚C
810 overnight. The samples were further fixed in 1% osmium in 0.1M PHEM buffer, washed in
811 water, and incubated in 1% uranylacetate in water overnight at 4˚C. Dehydration was done in
812 10 min steps in an acetone gradient followed by stepwise Spurr resin infiltration at room
813 temperature and polymerization at 60˚C.The blocks were trimmed to get longitudinal sections
814 of the notochord. 70nm thick sections were obtained using a leica UC6 ultramicrotome (Leica
815 Microsystems, Vienna) and the sections were collected on Formvar-coated, copper slot grids
816 and thereafter post-stained with uranyl acetate and Reynold‘s lead citrate. Imaging was done
817 using a JEOL JEM-1400 electron microscope (JEOL, Tokyo) operating at 80 kV and equipped
818 with a 4K TemCam F416 (Tietz Video and Image Processing Systems GmBH, Gautig).

819

820 **Transcriptomics data and candidate picking**

821 The targeted genes were selected from single cell transcriptomics data generated by the Klein
822 Lab (Briggs et al., 2018) based on a number of different criteria. First, high enrichment during
823 early development of the notochord in zebrafish. Precisely, candidates were picked from 10,
824 14, 18 and 24 hpf data. Second, the selected genes were checked for conservation across
825 vertebrates. Third the genes had to be well annotated but poorly characterized in both Medaka

826 and Zebrafish. Lastly, a compact and short CDS, simple exon-intron structure/number and
827 limited alternative splicing was favoured to improve chances of efficient mutagenesis with the
828 CRISPR machinery.

829 **Bioinformatics tools**
830
831 ENSEMBL(www.ensembl.org) was used to obtain all the coding sequences and upstream
832 promoter regions for all genes analysed in this study. Supplementary Table 1 and 2 were
833 generated using standard ensembl software using the 1-1 and 1-many orthologue
834 comparisons. Genomic sequence alignments for synteny were performed on ensembl or using
835 GENOMICUS (www.genomicus.biologie.ens.fr/). Protein information and amino acid
836 sequence alignments were done using Uniprot (www.uniprot.org). UCSC
837 (https://genome.ucsc.edu/) genome browser was used for the identification of the promoter
838 region of desmogon. Pfam and PRINTS were used for information on protein domains and
839 conserved motifs (https://pfam.xfam.org/) (http://130.88.97.239/PRINTS/index.php). Single
840 cell transcriptomics data was visualized using
841 (https://kleintools.hms.harvard.edu/paper_websites/wagner_zebrafish_timecourse2018/sprin
842 gViewer.html?coarse_grained_tree) and the selected candidates were obtained from list of
843 enriched genes in developing Zebrafish notochords.

844
845
846
847
848
849
850
851
852
853
854
855
856
857
858
859
860

References

Adams, D.S. & Keller, R.E., Koehl, M.A.R 1990. Mechanical Development of the Notochord in Xenopus Early Tail-Bud Embryos. In *Biomechanics of Active Movement and Deformation of Cells*. Berlin, Heidelberg: Springer Berlin Heidelberg, pp. 471–485.

Briggs, J.A. et al., 2018. The dynamics of gene expression in vertebrate embryogenesis at single-cell resolution. *Science*, 360(6392), pp.eaar5780–17.

Corallo, D., Trapani, V. & Bonaldo, P., 2018. The notochord: structure and functions. *Cellular and Molecular Life Sciences*, pp.1–20.

Dale, R.M. & Topczewski, J., 2011. Identification of an evolutionarily conserved regulatory element of the zebrafish col2a1a gene. *Developmental Biology*, 357(2), pp.518–531.

Delva, E., Tucker, D.K. & Kowalczyk, A.P., 2009. The desmosome. *Cold Spring Harbor Perspectives in Biology*, 1(2), pp.a002543–a002543.

Ellis, K., Bagwell, J. & Bagnat, M., 2013. Notochord vacuoles are lysosome-related organelles that function in axis and spine morphogenesis. *The Journal of Cell Biology*, 200(5), pp.667–679.

Ellis, K., Hoffman, B.D. & Bagnat, M., 2014. The vacuole within. *BioArchitecture*, 3(3), pp.64–68.

Farrell, J.A. et al., 2018. Single-cell reconstruction of developmental trajectories during zebrafish embryogenesis. *Science*, 360(6392), pp.eaar3131–15.

Fleming, A., 2004. A central role for the notochord in vertebral patterning. *Development*, 131(4), pp.873–880.

Fouquet, B. et al., 1997. Vessel Patterning in the Embryo of the Zebrafish: Guidance by Notochord. *Developmental Biology*, 183(1), pp.37–48.

Garcia, J. et al., 2017. Sheath Cell Invasion and Trans-differentiation Repair Mechanical Damage Caused by Loss of Caveolae in the Zebrafish Notochord. *Current Biology*, 27(13), pp.1982–1989.e3.

Garrod, D. & Chidgey, M., 2008a. Desmosome structure, composition and function. *Biochimica et Biophysica Acta (BBA) - Biomembranes*, 1778(3), pp.572–587.

Garrod, D. & Chidgey, M., 2008b. Desmosome structure, composition and function. *Biochimica et Biophysica Acta (BBA) - Biomembranes*, 1778(3), pp.572–587.

Goonesinghe, A. et al., 2012. Desmosomal cadherins in zebrafish epiboly and gastrulation. *BMC Developmental Biology*, 12(1), p.1.

Gray, R.S. et al., 2014. Loss of col8a1a function during zebrafish embryogenesis results in congenital vertebral malformations. *Developmental Biology*, 386(1), pp.72–85.

Hebrok, M., Kim, S.K. & Melton, D.A., 1998. Notochord repression of endodermal Sonic hedgehog permits pancreas development. *Genes & Development*, 12(11), pp.1705–1713.

900 Ito, K. et al., 2014. Differential reparative phenotypes between zebrafish and medaka after
901 cardiac injury. *Developmental Dynamics*, 243(9), pp.1106–1115.

902 Jiang, D. & Smith, W.C., 2007. Ascidian notochord morphogenesis. *Developmental*
903 *Dynamics*, 236(7), pp.1748–1757.

904 Kaloulis, K. et al., 2004. Reactivation of developmental programs: the cAMP-response
905 element-binding protein pathway is involved in hydra head regeneration. *Proceedings of*
906 *the National Academy of Sciences*, 101(8), pp.2363–2368.

907 Kang, J. et al., 2016. Modulation of tissue repair by regeneration enhancer elements. *Nature*,
908 532(7598), pp.201–206.

909 Katogi, R. et al., 2004. Large-scale analysis of the genes involved in fin regeneration and
910 blastema formation in the medaka, Oryzias latipes. *Mechanisms of Development*, 121(7-
911 8), pp.861–872.

912 Koehl, M.A.R., Quillin, K.J. & Pell, C.A., 2000. Mechanical Design of Fiber-Wound Hydraulic
913 Skeletons: The Stiffening and Straightening of Embryonic Notochords. *American*
914 *Zoologist*, 40(1), pp.28–041.

915 Krzic, U., Gunther, S., Saunders, T.E., Streichan, S.J. & Hufnagel, L., 2012a. Multiview light-
916 sheet microscope for rapid in toto imaging. *Nature methods*, 9(7), pp.730–733.

917 Krzic, U., Gunther, S., Saunders, T.E., Streichan, S.J. & Hufnagel, L., 2012b. Multiview light-
918 sheet microscope for rapid in toto imaging. *Nature methods*, 9(7), pp.730–733.

919 Lai, S.-L. et al., 2017. Reciprocal analyses in zebrafish and medaka reveal that harnessing
920 the immune response promotes cardiac regeneration. *eLife*, 6, p.1382.

921 Lim, Y.-W. et al., 2017. Caveolae Protect Notochord Cells against Catastrophic Mechanical
922 Failure during Development. *Current Biology*, 27(13), pp.1968–1981.e7.

923 Lischik, C.Q., Adelmann, L. & Wittbrodt, J., 2018. Enhanced in vivo-imaging in fish by
924 optimized anaesthesia, fluorescent protein selection and removal of pigmentation.

925 Lleras Forero, L. et al., 2018. Segmentation of the zebrafish axial skeleton relies on
926 notochord sheath cells and not on the segmentation clock. *eLife*, 7, p.15.

927 LoCascio, S.A., Lapan, S.W. & Reddien, P.W., 2017. Eye Absence Does Not Regulate
928 Planarian Stem Cells during Eye Regeneration. *Developmental Cell*, 40(4), pp.381–
929 391.e3.

930 Lopez-Baez, J.C. et al., 2018. Wilms Tumor 1b defines a wound-specific sheath cell
931 subpopulation associated with notochord repair. *eLife*, 7, p.239.

932 Lust, K. & Wittbrodt, J., 2018. Activating the regenerative potential of Müller glia cells in a
933 regeneration-deficient retina. *eLife*, 7, p.7028.

934 Melby, A.E., Warga, R.M. & Kimmel, C.B., 1996. Specification of cell fates at the dorsal
935 margin of the zebrafish gastrula. *Development*, 122(7), pp.2225–2237.

936 Nixon, S.J. et al., 2007. Caveolin-1 is required for lateral line neuromast and
937 notochord development. *Journal of Cell Science*, 120(13), pp.2151–2161.
938

939 Pourquie, O. et al., 1993. Control of dorsoventral patterning of somitic derivatives by
940 notochord and floor plate. *Proceedings of the National Academy of Sciences*, 90(11),

941 pp.5242–5246.

942 Rembold, M. et al., 2006. Transgenesis in fish: efficient selection of transgenic fish by co-
943 injection with a fluorescent reporter construct. *Nature protocols*, 1(3), pp.1133–1139.

944 Rodrigo Albors, A. et al., 2015. Planar cell polarity-mediated induction of neural stem cell
945 expansion during axolotl spinal cord regeneration. *eLife*, 4, p.664.

946 Satoh, N., Tagawa, K. & Takahashi, H., 2012. How was the notochord born? *Evolution &*
947 *Development*, 14(1), pp.56–75.

948 Seleit, A., Krämer, I., Ambrosio, E., et al., 2017. Sequential organogenesis sets two parallel
949 sensory lines in medaka. *Development*, 144(4), pp.687–697.

950 Seleit, A., Krämer, I., Riebesehl, B.F., et al., 2017. Neural stem cells induce the formation of
951 their physical niche during organogenesis. *eLife*, 6, p.505.

952 Stemmer, M., Schuhmacher, L.N., et al., 2015. Cavefish eye loss in response to an early
953 block in retinal differentiation progression. *Development*, 142(4), pp.743–752.

954 Stemmer, M., Thumberger, T., et al., 2015. CCTop: An Intuitive, Flexible and Reliable
955 CRISPR/Cas9 Target Prediction Tool. S. Maas, ed. *PloS one*, 10(4), p.e0124633.

956 Stemple, D.L., 2005. Structure and function of the notochord: an essential organ for chordate
957 development. *Development*, 132(11), pp.2503–2512.

958 Stemple, D.L., 2004. The notochord. *Current Biology*, 14(20), pp.R873–R874.

959 Stemple, D.L. et al., 1996. Mutations affecting development of the notochord in zebrafish.
960 *Development*, 123, pp.117–128.

961 Stoeger, T. et al., 2018. Large-scale investigation of the reasons why potentially important
962 genes are ignored. T. Freeman, ed. *PLOS Biology*, 16(9), p.e2006643.

963 Tada, M. & Heisenberg, C.P., 2012. Convergent extension: using collective cell migration
964 and cell intercalation to shape embryos. *Development*, 139(21), pp.3897–3904.

965 Talbot, W.S. et al., 1995. A homeobox gene essential for zebrafish notochord development.
966 *Nature*, 378(6553), pp.150–157.

967 Tanaka, E. & Galliot, B., 2009. Triggering the regeneration and tissue repair programs. In
968 Development (Cambridge, England). pp. 349–353.

969 Trubiroha, A. et al., 2018. A Rapid CRISPR/Cas-based Mutagenesis Assay in Zebrafish for
970 Identification of Genes Involved in Thyroid Morphogenesis and Function. *Scientific*
971 *Reports*, pp.1–19.

972 Van Wettere, A.J. et al., 2013. Immunohistochemical characterization of the hepatic
973 progenitor cell compartment in medaka (Oryzias latipes) following hepatic injury. *Journal*
974 *of comparative pathology*, 149(4), pp.434–445.

975 Wopat, S. et al., 2018. Spine Patterning Is Guided by Segmentation of the Notochord
976 Sheath. *CellReports*, 22(8), pp.2026–2038.

977 Wu, R.S. et al., 2018. A Rapid Method for Directed Gene Knockout for Screening in G0
978 Zebrafish. *Developmental Cell*, 46(1), pp.112–125.e4.

Yamada, T. et al., 1991. Control of cell pattern in the developing nervous system: Polarizing activity of the floor plate and notochord. *CELL*, 64(3), pp.635–647.

Yamada, T. et al., 1993. Control of cell pattern in the neural tube: Motor neuron induction by diffusible factors from notochord and floor plate. *CELL*, 73(4), pp.673–686.

Yamamoto, M. et al., 2010. Mib-Jag1-Notch signalling regulates patterning and structural roles of the notochord by controlling cell-fate decisions. *Development*, 137(15), pp.2527–2537.

Acknowledgments

We would like to thank Sylvia Urbansky and Steffen Lemke for critical input on the manuscript. J. Wittbrodt for the use of confocal and light sheet microscopes and generous support. We would like to thank C. Funaya, S. Gold and S. Hillmer from the EMCF facility at Heidelberg University for the preparation, imaging and processing of the electron microscopy data. We would like to thank Nihad Softic for injections for spare labeling and Pui Oui Hong for help with the genotyping of Desmogon mutants. We thank E. Leist, M. Majewski and A. Saraceno for fish husbandry.

Funding

Deutsche Forschungsgemeinschaft (SFB 873)

- Ali Seleit
- Karen Gross
- Lazaro Centanin

The funders had no role in study design, data collection and interpretation, or the decision to submit the work for publication.

Competing interests

No competing interests

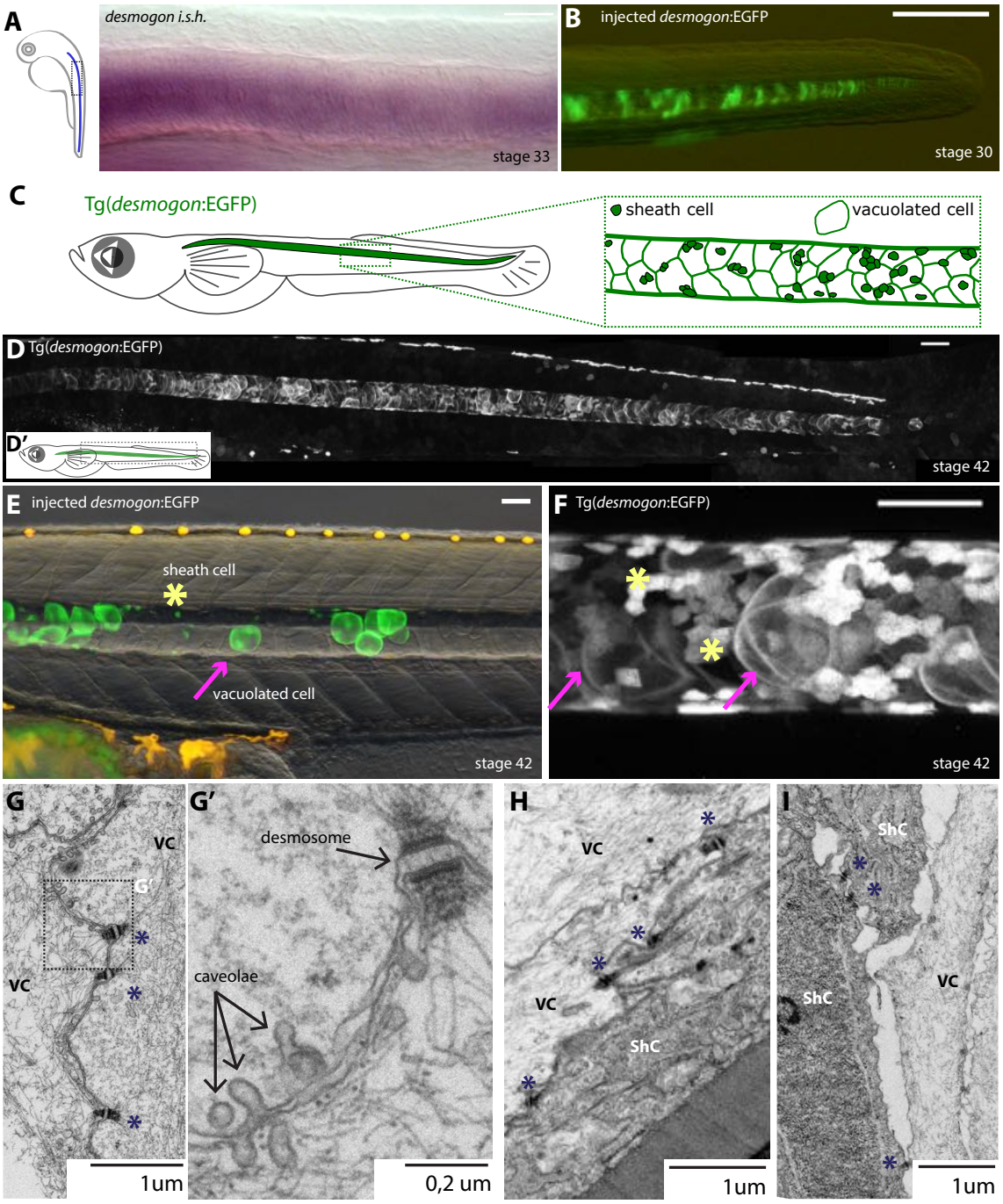

Seleit et al, Figure 1

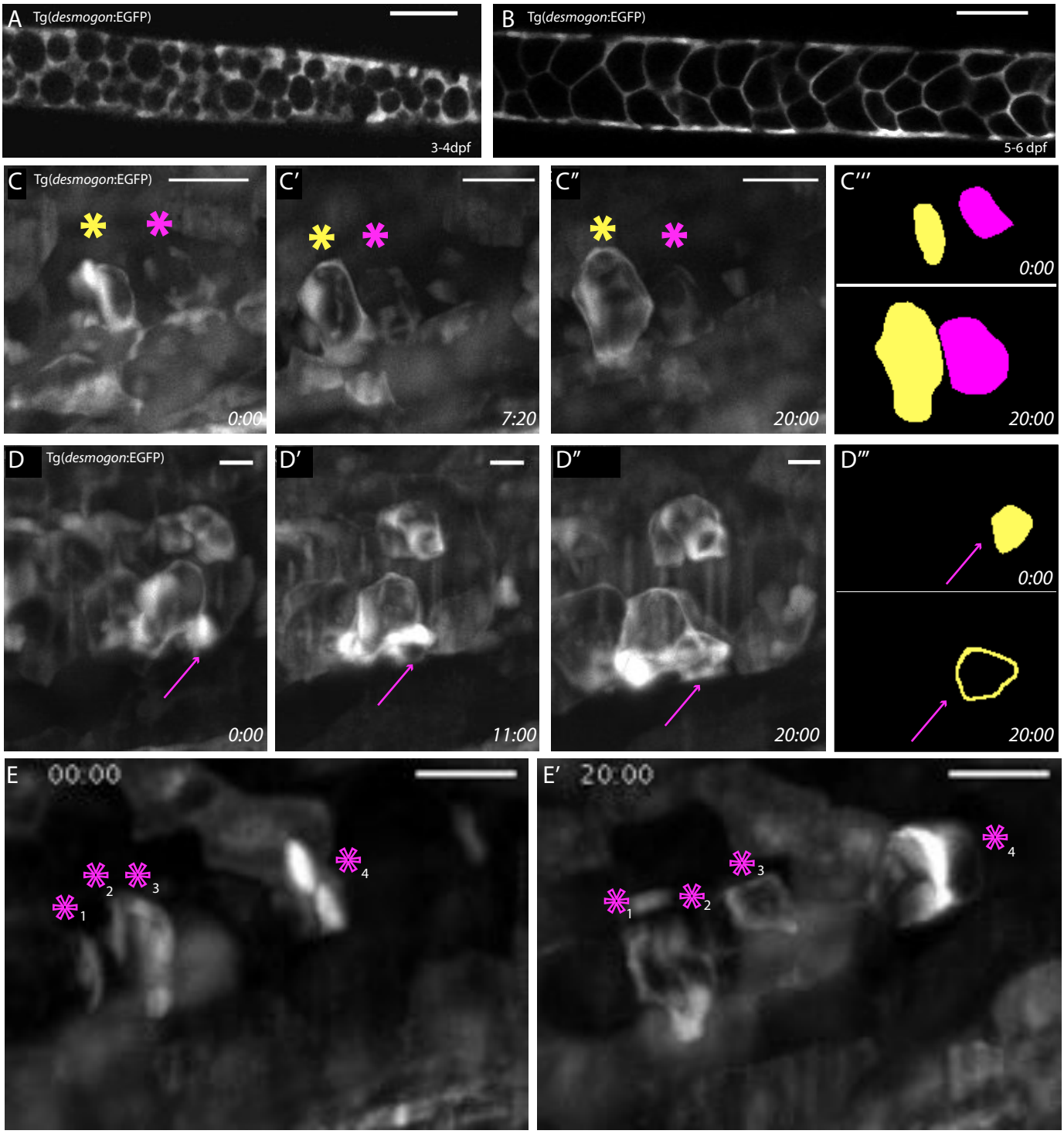

Seleit et al, Figure 2

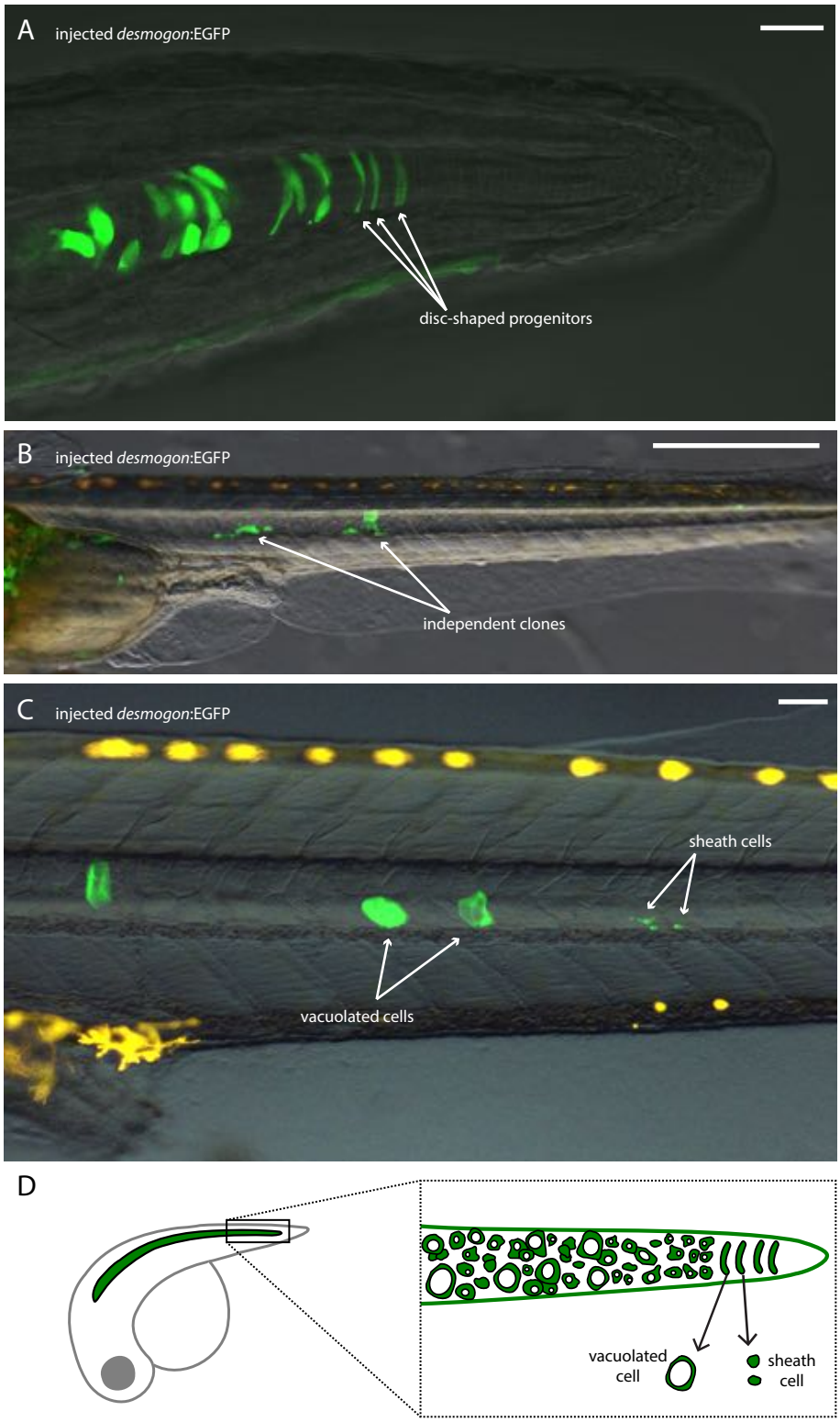

Seleit et al, Figure 3

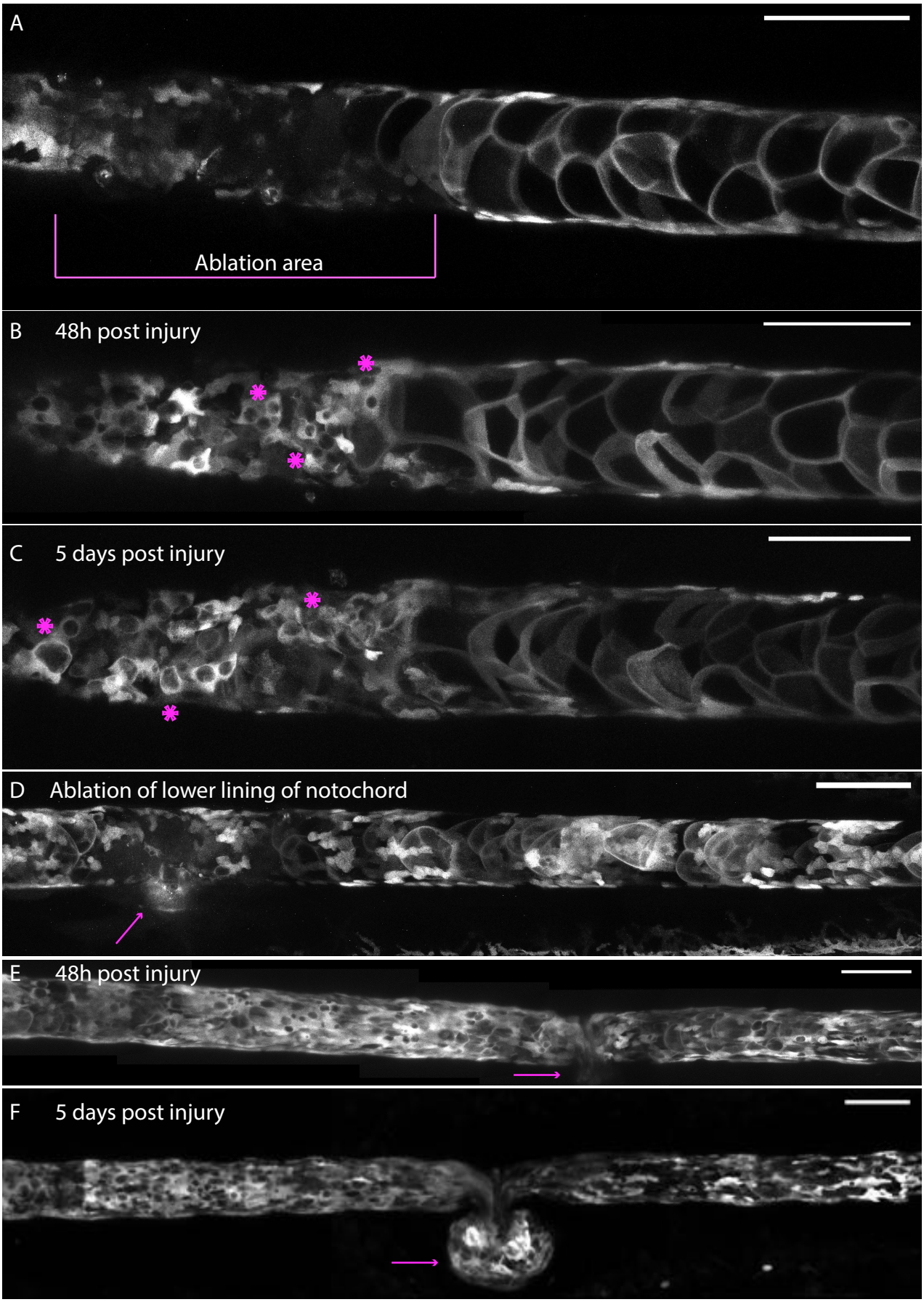

Seleit et al, Figure 4

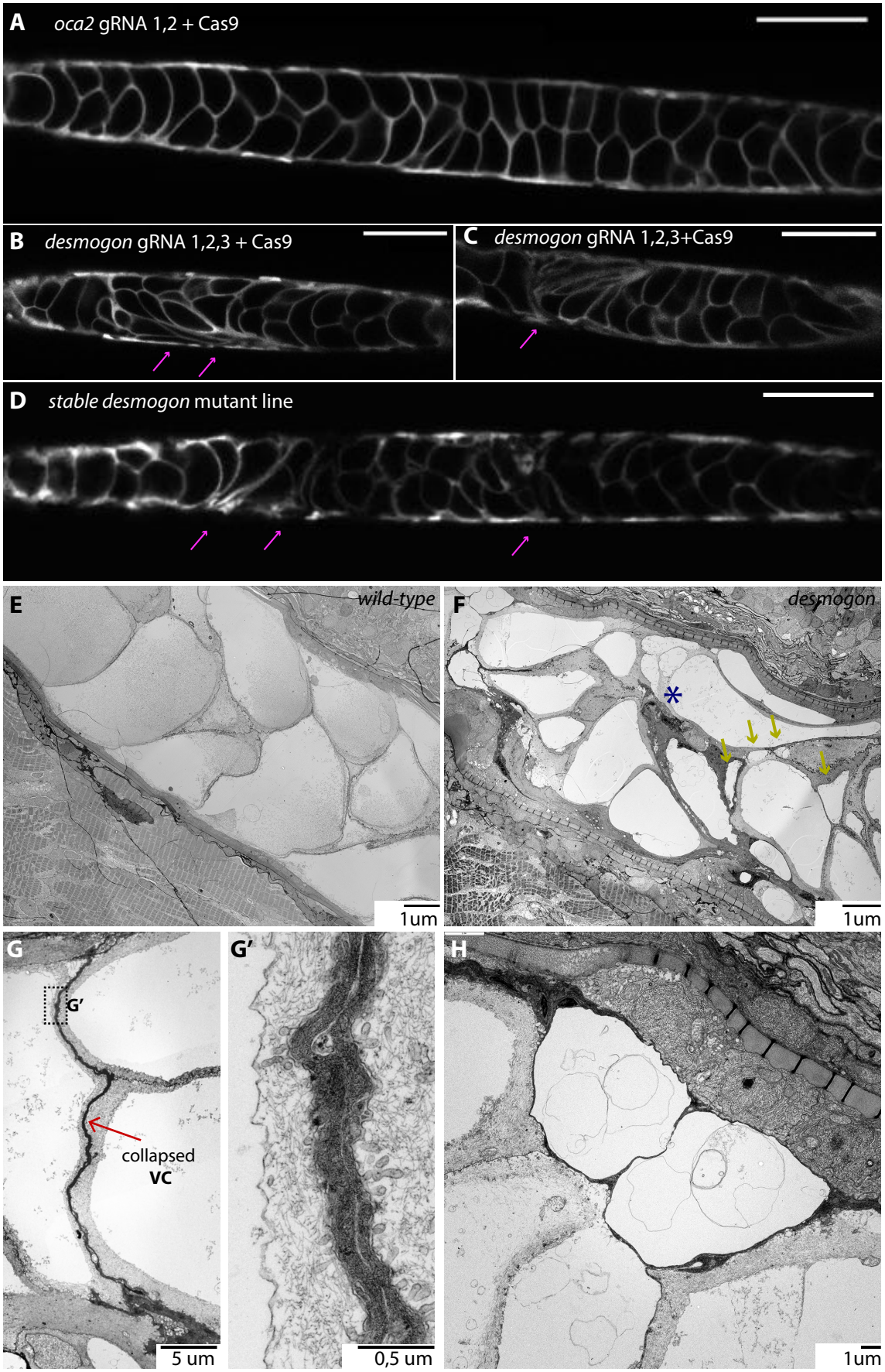

Seleit et al, Figure 5

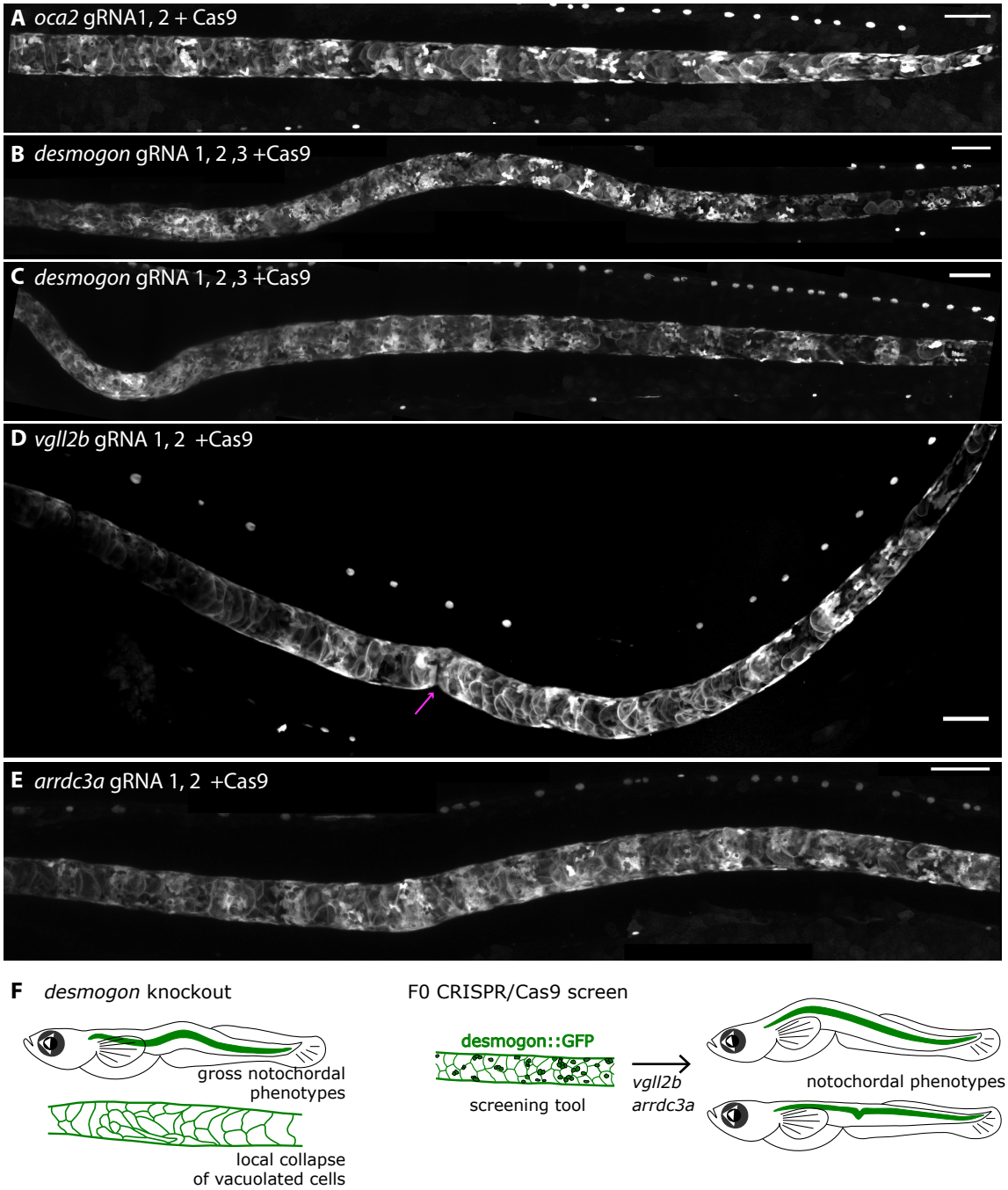

Seleit et al, Figure 6

Gene Name	**Full name**	**proposed roles structure and localization**	**CRISPR Injected F0 Phenotypes %**	**Phenotypic description**
dsgon	*desmogon*	constituent of desmosomal structures, plasma membrane	40,6	local collapses of vacuolated cells, notochord bending, local notochord collapses, no pleotropic effects, highly specific to notochord, 90% of embryos survive to stage 42
vgll2b	*vestigial-like family member 2b*	predicted transcription factor TF/co-factor, nuclear	55	strong phenotypes in the notochord, bending and twisted notochords, spirals of notochord, notochord tube coiling, local collapses of notochord no big pleotropic effects, 79% of embryos survive to stage 42
arrdc3a	*arrestin domain containing 3a*	regulating signal transduction at G protein-coupled receptors	30	wavy notochords, twisted notochords, no strong pleiotropic effects, 77% of embryos survive to stage 42
kcnk6	*potassium two pore domain channel subfamily K member 6*	ion transport, plasma membrane	44,3	kinks and wavy notochords, shorter axis elongation, general growth retardation 73% survive to stage 42
si:dkey-261h17.1	ENSORLG00000015828	cell adhesion, membrane bound	42,1	notochord spirals and twists, wavy notochord, kinks, perturbed axis elongation, 69% of embryos survive to stage 42
pmp22b	*peripheral myelin protein 22b*	helical transmembarne, integral component of membranes,	31,2	strong pleiotropic effects, growth retardation and developmental delays, heart edemas, smaller eyes, wavy notochords, spiral notochords and twists, short axis/failure of axis extension, patterning defects, 58% survive to stage 42

Supplementary figure 1

A

Species	Protein name	Protein entry	Sequence identity %
Oryzias latipes	uncharacterized	H2MRM9	100,0
Fundulus heteroclitus	uncharacterized	A0A147B2M0	66,7
Poeciliopsis prolifica	DSG2	A0A0S7JQR1	65,0
Xiphophorus maculatus	uncharacterized	M4AQR9	59,9
Nothobranchius furzeri	uncharacterized	A0A1A7ZRJ5	59,5
Astyanax mexicanus	uncharacterized	W5KFL2	59,5
Poecilia formosa	uncharacterized	A0A087X6J9	57,3
Danio rerio	dsg2.1	H2EQR6	46,6
Xenopus laevis	dsg2	A0A1L8FYU6	41,6
Homo sapiens	DSG2	Q14126	40,2
Gallus gallus	DSG2	F1NJD5	40,0
Mus musculus	Dsg2	O55111	39,2
Rattus norvegicus	Dsg2	F1LYX9	38,7

B

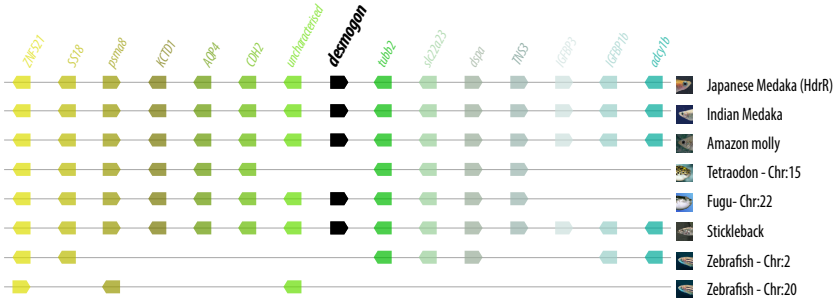

C

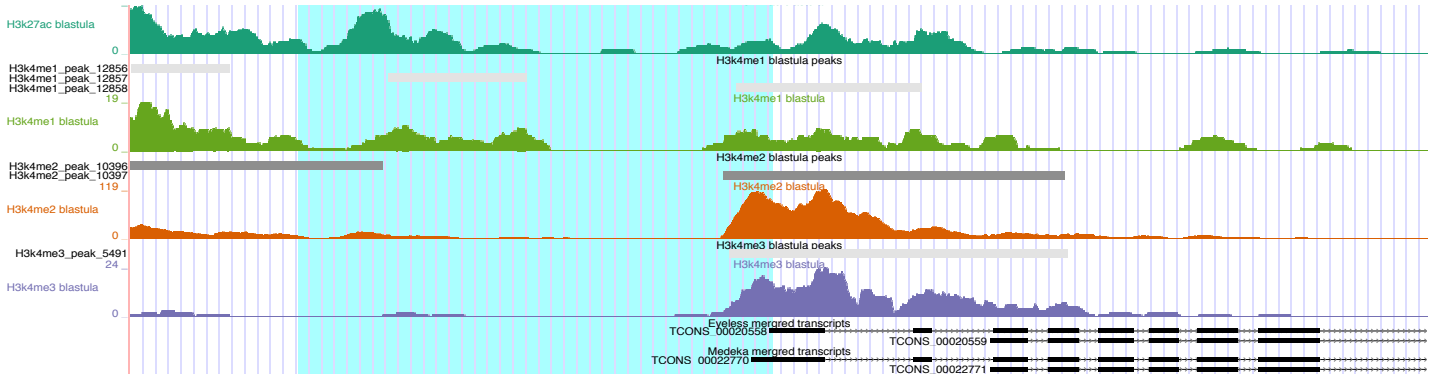

Supplementary Figure 2

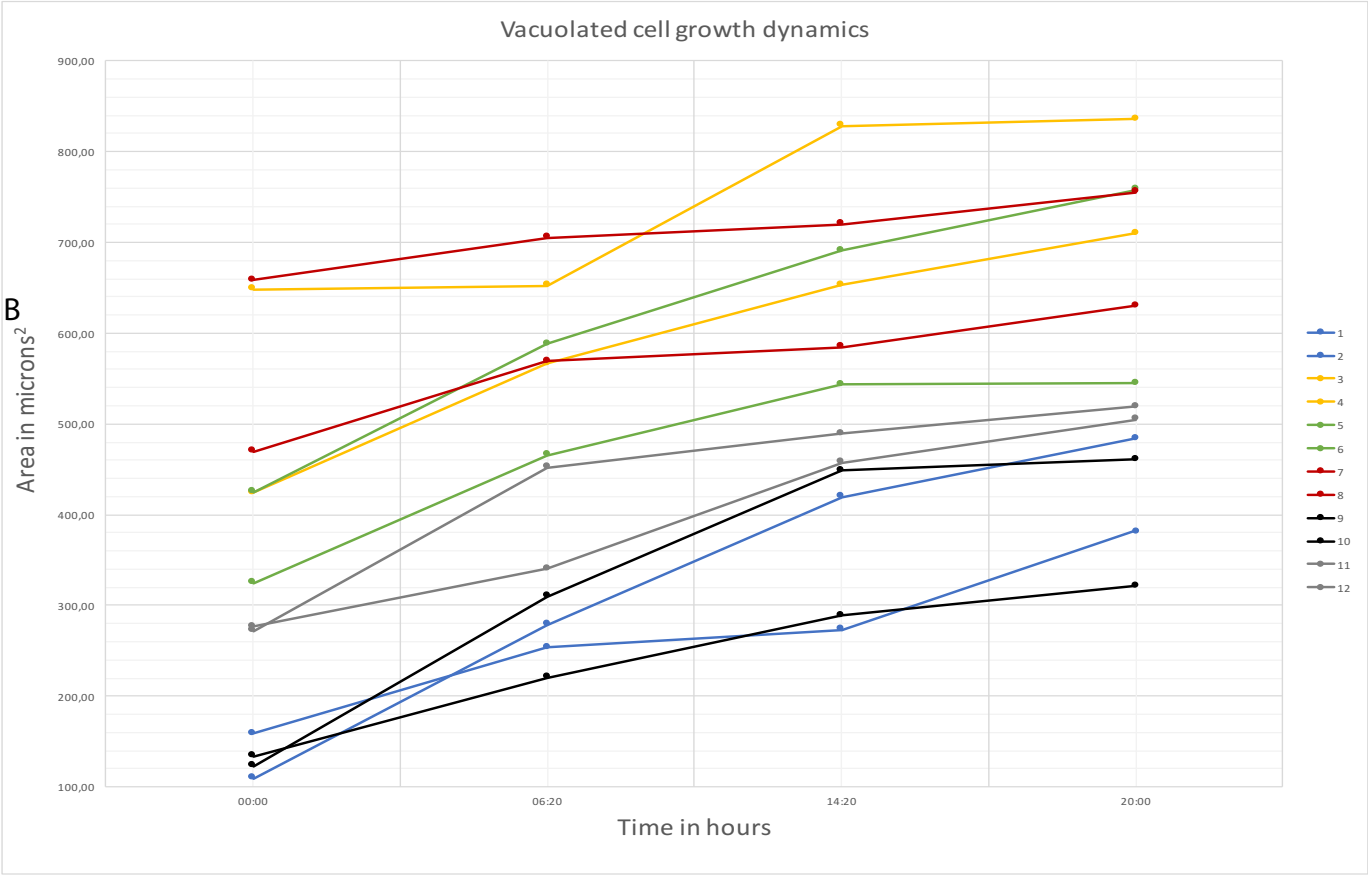

Supplementary Figure 3

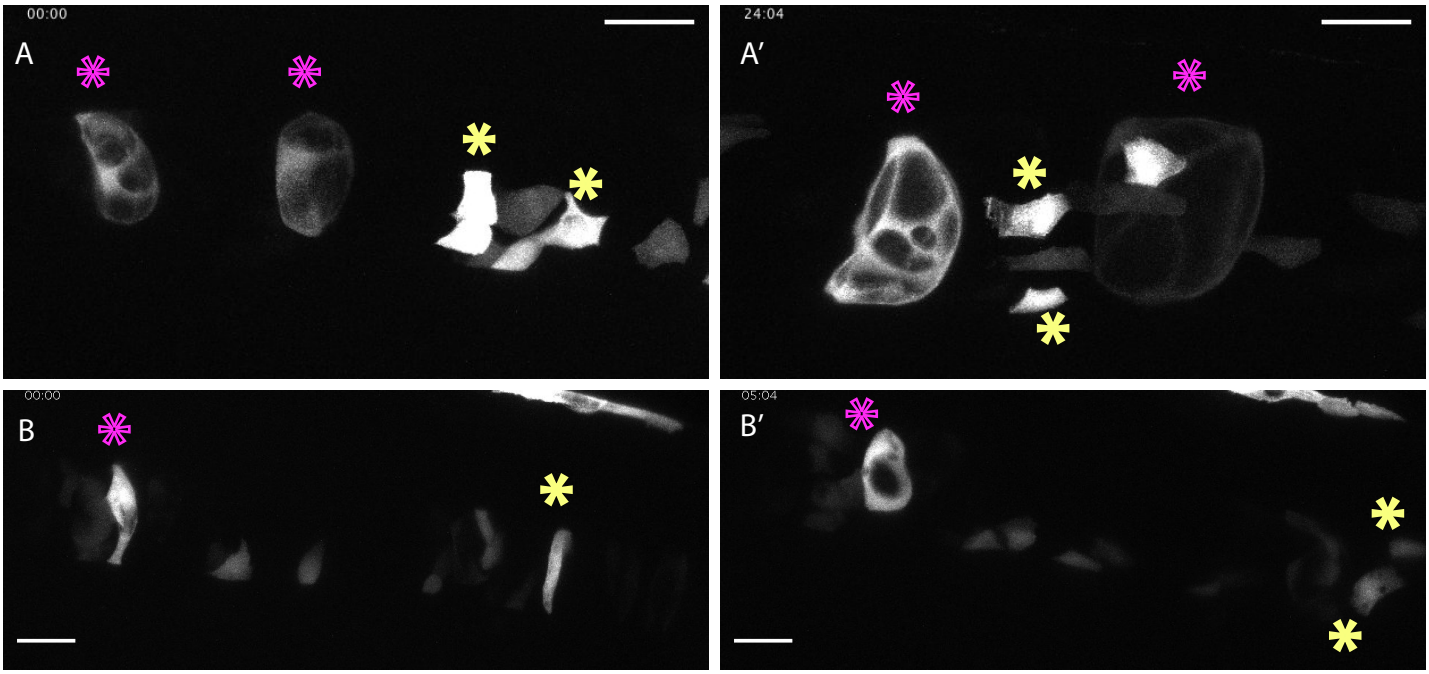

Supplementary Figure 4

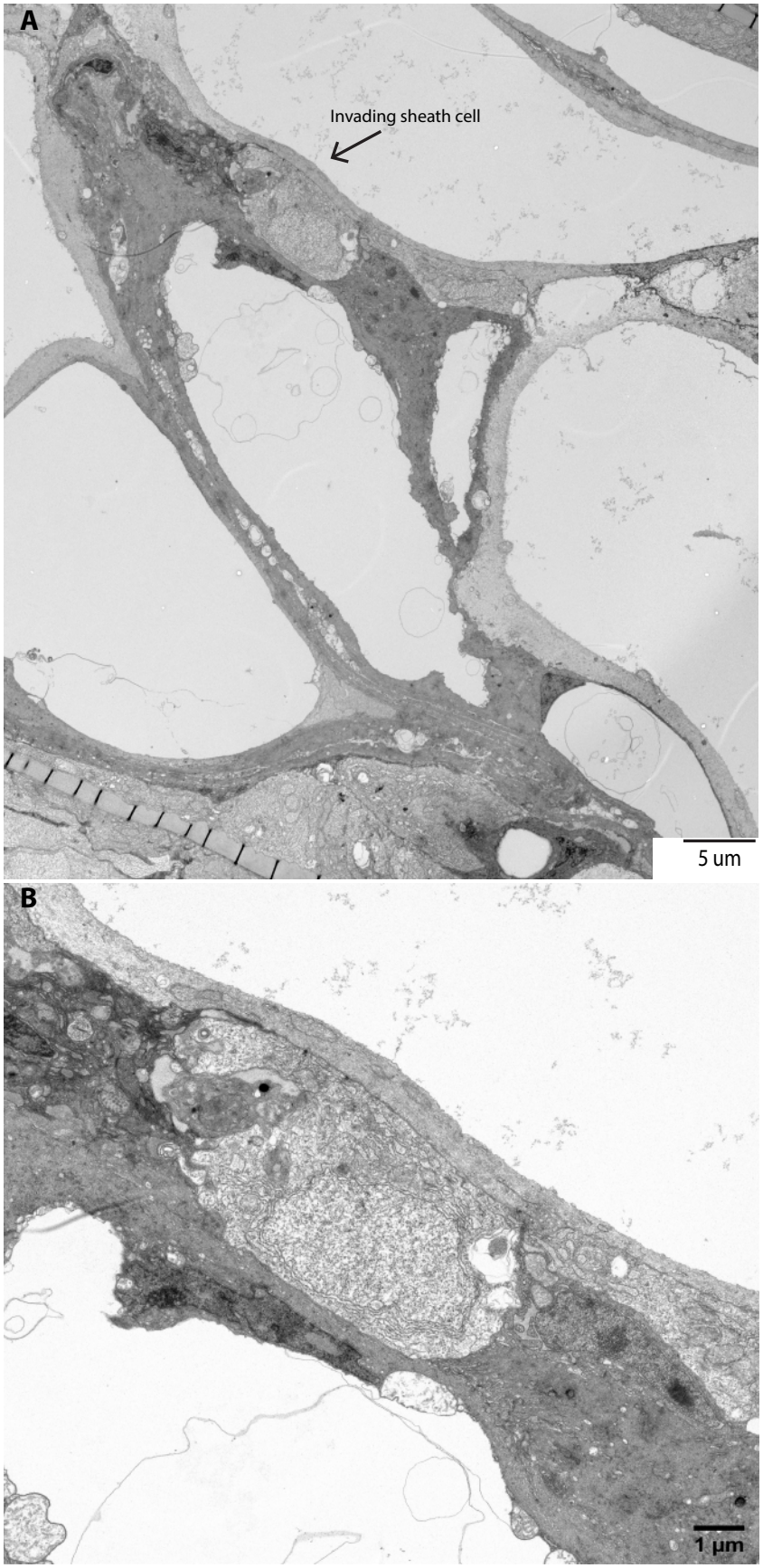

Supplementary Figure 5

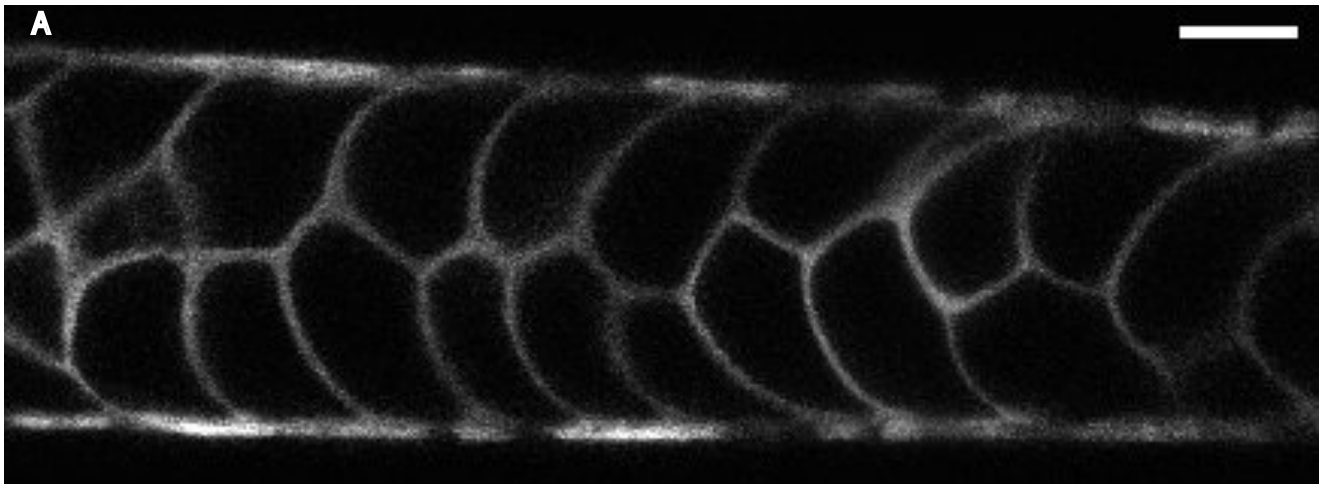

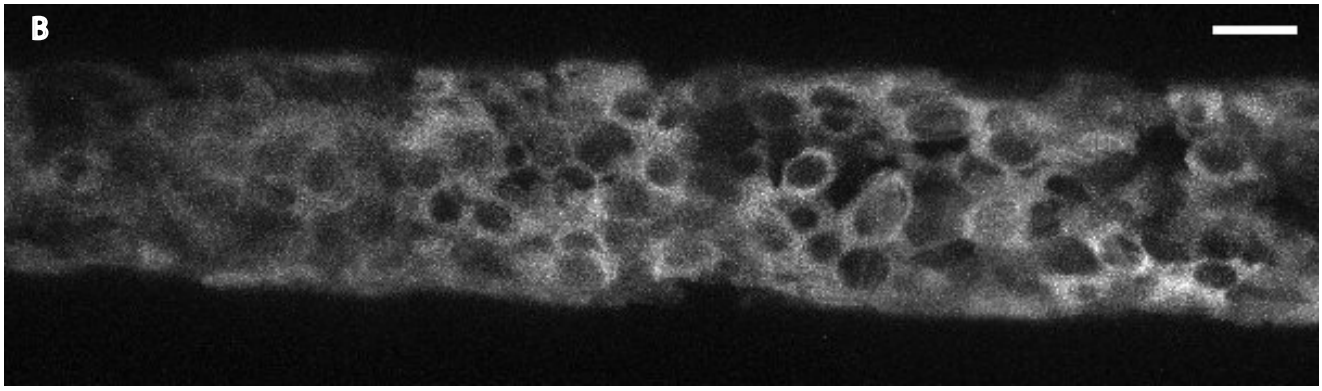

C

Species	Protein name	Protein entry	Sequence identity %
Oryzias latipes	vgll2b	H2MAV4	100
Nothobranchius furzeri	VGLL2B	A0A1A8B070	87,2
Poecilia formosa	uncharacterized	A0A087XF56	78,6
Xiphophorus maculatus	uncharacterized	M4AFN1	77,6
Danio rerio	vgll2b	Q499A6	66
Lepisosteus oculatus	uncharacterized	W5MDI3	57,4
Astyanax mexicanus	uncharacterized	W5KS66	56,5
Gallus gallus	VGLL2	C0KDW3	40,7
Mus musculus	Vgll2	Q8BGW8	38,7
Homo sapiens	VGLL2	Q8N8G2	38

D

Species	Protein name	Protein entry	Sequence identity %
Oryzias latipes	arrdc3a	H2M3K3	100
Oreochromis niloticus	arrdc3	I3K178	96,4
Tetraodon nigroviridis	arrdc3a	H3CX04	95,4
Xiphophorus maculatus	uncharacterized	M4AYA0	93
Poeciliopsis prolifica	ARRD3	A0A0S7HB53	92,7
Astyanax mexicanus	uncharacterized	W5L537	92
Danio rerio	arrdc3a	Q1ECU3	89,9
Gallus gallus	ARRDC3	R4GLF2	85,6
Mus musculus	Arrdc3	Q7TPQ9	85,3
Homo sapiens	ARRDC3	Q96B67	84,8